POLYPUBLIE
Polytechnique Montréal

POLYTECHNIQUE MONTRÉAL
UNIVERSITÉ D'INGÉNIERIE

Titre: Title: Meso-scale numerical analysis of the role of Van der Waals adhesion and static friction in fluidized beds of fine solids

Auteurs: Authors: Youssef Badran, Dorian Dupuy, Bruno Blais, Vincent Moureau, Renaud Ansart, Jamal Chaouki, & Olivier Simonin

Date: 2025

Type: Article de revue / Article

Référence: Citation: Badran, Y., Dupuy, D., Blais, B., Moureau, V., Ansart, R., Chaouki, J., & Simonin, O. (2025). Meso-scale numerical analysis of the role of Van der Waals adhesion and static friction in fluidized beds of fine solids. Powder Technology, 455, 120763 (15 pages). https://doi.org/10.1016/j.powtec.2025.120763

Document en libre accès dans PolyPublie
Open Access document in PolyPublie

URL de PolyPublie: PolyPublie URL: https://publications.polymtl.ca/62755/

Version: Version officielle de l'éditeur / Published version
Révisé par les pairs / Refereed

Conditions d'utilisation: Terms of Use: Creative Commons Attribution-Utilisation non commerciale-Pas d'oeuvre dérivée 4.0 International / Creative Commons Attribution-NonCommercial-NoDerivatives 4.0 International (CC BY-NC-ND)

Document publié chez l'éditeur officiel
Document issued by the official publisher

Titre de la revue: Journal Title: Powder Technology (vol. 455)

Maison d'édition: Publisher: Elsevier

URL officiel: Official URL: https://doi.org/10.1016/j.powtec.2025.120763

Mention légale: Legal notice: ©2025 The Authors. Published by Elsevier B.V. This is an open access article under the CC BY-NC-ND license (http://creativecommons.org/licenses/bync-nd/4.0/).

Ce fichier a été téléchargé à partir de PolyPublie, le dépôt institutionnel de Polytechnique Montréal
This file has been downloaded from PolyPublie, the institutional repository of Polytechnique Montréal

https://publications.polymtl.ca

Powder Technology 455 (2025) 120763

Contents lists available at ScienceDirect

Powder Technology

journal homepage: www.journals.elsevier.com/powder-technology

Meso-scale numerical analysis of the role of Van der Waals adhesion and static friction in fluidized beds of fine solids

Youssef Badran [a,b], Dorian Dupuy [a], Bruno Blais [e], Vincent Moureau [d], Renaud Ansart [a], Jamal Chaouki [b], Olivier Simonin [c,*]

[a] Laboratoire de Génie Chimique, Université de Toulouse, CNRS, INPT, UPS, Toulouse, France
[b] Process Engineering Advanced Research Lab (PEARL), Department of Chemical Engineering, Polytechnique Montréal, P.O. Box 6079, Station Centre-ville, Montréal, Québec H3C 3A7, Canada
[c] Institut de Mécanique des Fluides de Toulouse (IMFT), Université de Toulouse, CNRS, Toulouse, France
[d] CORIA UMR 6614 CNRS-INSA, Université de Rouen, 76801 Saint-Etienne du Rouvray, France
[e] CHAOS Laboratory, Department of Chemical Engineering, Polytechnique Montréal, P.O. Box 6079, Station Centre-ville, Montréal, Québec H3C 3A7, Canada

HIGHLIGHTS

- Van der Waals forces cause pressure overshoot in fluidized beds of fine particles.
- Static wall friction also contributes to the pressure-drop overshoot.
- Van der Waals adhesion is crucial for predicting homogeneous bed expansion.
- Gas flow rate and Van der Waals forces impact the evolution of particle contacts.
- A CFD-DEM database is generated to guide developing continuum solid stress closures.

GRAPHICAL ABSTRACT

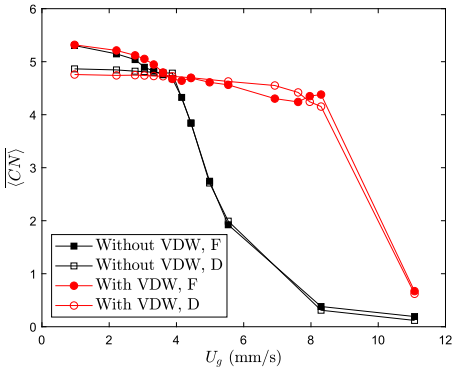

Predicting the homogeneous fluidization regime by accounting for Van der Waals (VDW) adhesion: mean number of contacts per particle versus superficial gas velocity for defluidization (D) and fluidization (F) cycles.

ARTICLE INFO

Keywords:
Gas–solid fluidized beds
Van der Waals adhesion
Static-dynamic friction
Pressure-drop hysteresis
Homogeneous fluidization
CFD-DEM

ABSTRACT

This article explores the effect of Van der Waals force and static friction on the fluidization of fine solids using CFD-DEM simulations. The results show that both Van der Waals adhesion and static friction contribute to the pressure-drop hysteresis phenomenon. These results also demonstrate that to predict the homogeneous expansion of the bed across the range of velocities from the minimum required for fluidization to the minimum for bubbling, it is necessary to take into account the Van der Waals adhesion. The generated CFD-DEM dataset can guide the development of solid stress closures for two-fluid models to incorporate the effects of Van der Waals adhesion and static friction on fluidization hydrodynamics, allowing for the prediction of hysteresis in bed pressure drop at the macro-scale.

* Corresponding author.
E-mail address: olivier.simonin@toulouse-inp.fr (O. Simonin).

https://doi.org/10.1016/j.powtec.2025.120763
Received 25 September 2024; Received in revised form 27 January 2025; Accepted 6 February 2025
Available online 15 February 2025
0032-5910/© 2025 The Authors. Published by Elsevier B.V. This is an open access article under the CC BY-NC-ND license (http://creativecommons.org/licenses/by-nc-nd/4.0/).

1. Introduction

Fluidized and packed (fixed or moving) beds are used in several industrial processes and applications, including the chemical, pharmaceutical, food, and mining industries [1–5]. Both fixed and fluidized beds have their own advantages and disadvantages [2,6,7]. Studying the hydrodynamics of these beds and developing numerical models able to predict the different transport phenomena occurring inside them can play a key role in their optimization and scale-up.

Several authors studied the role of friction and Van der Waals adhesion in fluidized beds. Dupuy et al. [8] showed through numerical simulations that friction hinders the dense packing of particles and plays a role in determining the minimum fluidization velocity. Zhang et al. [9] demonstrated, through Eulerian–Lagrangian simulations, that Van der Waals adhesion can lead to the aggregation of particles. Mutsers and Rietema [10] and Tsinontides and Jackson [11] hypothesized that the homogeneous fluidization observed in experiments with fine particles is caused by the adhesion and friction between these particles in contact. Rietema and Piepers [12] attributed the overshoot in the pressure drop across a bed of fine solids to particle–particle Van der Waals adhesion, as well as frictional interactions between the particles and the wall. Srivastava and Sundaresan [13] linked the larger overshoot they observed in smaller columns to particle–wall frictional interactions. The non-sphericity of particles increases interparticle and particle–wall friction, and amplifies the hysteresis in bed pressure drop [8,14–17].

The CFD-DEM (Computational Fluid Dynamics-Discrete Element Method) approach may be used to investigate fluid–solid flows in lab-scale fluidized beds containing typically the order of 10^6 particles [18,19], whereas the two-fluid approach can be employed to simulate industrial-scale fluidized beds [20]. A main advantage of the CFD-DEM approach over the two-fluid model is its ability to account for multiple and long-duration particle contacts. The assumption of binary and instantaneous collisions and the lack of proper solid stress closures render the two-fluid model incapable of predicting several phenomena that occur in dense granular media, such as the Janssen effect in silos [21] and the pressure-drop hysteresis in fine-particle fluidized beds [22–24]. Numerical data from CFD-DEM simulations may be employed to develop particle stress closures for the two-fluid model, allowing it to handle very dense fluid–solid flows with increased accuracy.

Several researchers used mesoscopic simulation data from DEM or CFD-DEM to compute macroscopic quantities and develop continuum models. Dupuy et al. [25] developed a continuum model for the particle–wall contact shear stress through analysis of CFD-DEM simulations. Rothenburg and Kruyt [26] carried out and analyzed various DEM simulations of 2D granular arrangements of disks undergoing biaxial compression. Based on their analysis, they postulated a transport equation for the coordination number, which contains empirical parameters that indicate probabilities of contact formation and destruction. They found that the theoretical solution of this transport equation is in good agreement with the DEM simulation data. According to their investigation, variations in solid fraction cannot be described only in terms of coordination number but also in terms of anisotropy in contact orientations. Sun and Sundaresan [27] used DEM simulations as a basis to develop closures for the solid pressure and the macroscopic friction coefficient in simple shear flows. These authors proposed continuum transport equations for the coordination number and the fabric tensor, which are included in the aforementioned closures. The material parameters in their constitutive model were calibrated to produce the desired response given by the DEM data. Chialvo et al. [28] studied simple shear flows of noncohesive particles through DEM simulations. They investigated three different flow regimes: inertial (dilute), intermediate, and quasistatic, as well as the transitions between them. For each flow regime, they found an asymptotic power-law relation between the particle pressure and the shear rate scaled by powers of the distance to the jamming point (separating the inertial and quasistatic regimes). This jamming point is affected by particle–particle friction. They also proposed a function that combines the previously mentioned asymptotic relationships, resulting in a continuous evolution of the solid pressure as a function of shear rate for the limits of the three flow regimes and the transitions between them. Luding [29] obtained macroscopic data such as bulk moduli, friction angle, and cohesion from DEM simulations of non-cohesive and cohesive particles subjected to a shear deformation. In his study, the macroscopic stress, stiffness, and fabric tensors were calculated. Gu et al. [30] modified the solid pressure and viscosity closures that are based on the kinetic theory to take adhesion into consideration. These modifications were guided by the results obtained from their CFD-DEM simulations. These researchers observed larger aggregates in a test with adhesion compared to a test without adhesion. Hou et al. [31] performed CFD-DEM simulations of fluidized beds with Geldart B and A particles accounting for the Van der Waals adhesion. Based on their mesoscopic data, they proposed correlations for the static, expanded, and fluidized bed states, which describe how the average number of contacts per particle varies with the particle volume fraction (macroscopic quantities). Vijayan et al. [32] used DEM to study the variation in the coordination number and contact anisotropy (fabric) for a 3D particle arrangement under uniaxial compression. They noticed a hysteresis between loading and unloading coordination number-strain curves. These authors defined three different flow regimes (quasi-static, dense, and collisional dilute) according to the value of the inertial number, which is expressed as a function of the compression strain rate and solid compressive pressure. They proposed a semi-empirical model that relates the contact anisotropy to the macroscopic stress.

Overall, Van der Waals and frictional interactions have a substantial effect on fluidization behavior. However, these interactions are not adequately modeled at the macroscale. Coupling mesoscopic and macroscopic scales is an effective strategy to address this issue. In this paper, we extract mesoscopic data from CFD-DEM simulations to guide the development of Eulerian solid stress closures for Van der Waals adhesion and friction. We implemented static-dynamic friction and Van der Waals adhesion models in the CFD-DEM code YALES2 [18]. Then, we used this code to perform Eulerian–Lagrangian simulations of fluidization and defluidization for Geldart A particles. From these simulations, we obtained information about the fluidization hydrodynamics and the structural and solid stress changes within the particle bed in the presence or absence of Van der Waals adhesion force. We show that both static friction and Van der Waals adhesion contribute to the pressure overshoot and that the homogeneous fluidization regime is only predicted when adhesion is present. Finally, we measure the source term in the coordination number transport equation. This source term is shown to be influenced by both the superficial gas velocity and Van der Waals adhesion force.

The paper is organized as follows: Section 2 briefly describes the modeling approach used in this research and explains the implementation of static-dynamic friction and Van der Waals adhesion in DEM, Section 3 presents the fluidization and defluidization CFD-DEM simulations conducted in this study and discusses the results obtained, and Section 4 covers the calculation of the source term of the Eulerian transport equation for the coordination number from CFD-DEM simulations.

2. Numerical model

A computational framework has been developed by integrating the DEM for particle phase representation and the LES (Large-Eddy Simulation) method for gas phase representation within the YALES2 code [18]. This computational tool uses the finite volume method and is designed to solve the filtered Navier–Stokes equations at low Mach numbers for flows with turbulence and chemical reactions. The LES equations for the gas phase can be found in Dufresne et al. [18]. These equations account for the local volume fraction of the gas, which is computed using the particle centroid method [33].

The motion of a spherical particle p, encompassing both translational and rotational aspects, can be determined through the application of Newton's second law [18]:

$$\mathrm{d}_t\left(\mathbf{x}_p\right) = \mathbf{u}_p, \tag{1}$$

$$m_p \mathrm{d}_t\left(\mathbf{u}_p\right) = \mathbf{F}_p^e + \mathbf{F}_p^c, \tag{2}$$

$$I_p \mathrm{d}_t\left(\boldsymbol{\omega}_p\right) = \mathbf{M}_p^d + \mathbf{M}_p^c + \mathbf{M}_p^r. \tag{3}$$

The variables I_p, m_p, $\mathbf{x}_p$, $\boldsymbol{\omega}_p$, and $\mathbf{u}_p$ denote respectively the moment of inertia, mass, position, angular velocity, and translation velocity of particle p. $\mathbf{F}_p^e$, $\mathbf{F}_p^c$, $\mathbf{M}_p^d$, $\mathbf{M}_p^c$, and $\mathbf{M}_p^r$ are respectively the overall external force acting upon particle p, the total contact force (due to inter-particle and particle–wall contacts), the torque of gas drag force, the torque of $\mathbf{F}_p^c$, and the torque due to rolling friction. The overall external force $\mathbf{F}_p^e$ encompasses the force of gravity $\mathbf{F}_p^g$ and the forces acting upon the solid by the gas, specifically the buoyancy force $\mathbf{F}_p^b$ and the drag force $\mathbf{F}_p^d$:

$$\mathbf{F}_p^e = \mathbf{F}_p^d + \mathbf{F}_p^b + \mathbf{F}_p^g. \tag{4}$$

Details about the modeling of the external force and the torques in Eqs. (2) and (3) can be found in the study by Nigmetova et al. [34] and in the thesis by Dufresne [35]. The contact forces are described in detail hereafter.

The Coulomb dynamic friction model relates the tangential and normal contact forces exerted by particle q on particle p as follows:

$$\mathbf{f}_{q\to p,t}^c = -\mu_d \|\mathbf{f}_{q\to p,n}^c\| \mathbf{t}_{pq}, \tag{5}$$

where μ_d is the dynamic (sliding) friction coefficient, $\mathbf{f}_{q\to p,n}^c$ is the normal contact force represented using a spring–dashpot system, and $\mathbf{t}_{pq}$ is the tangential unit vector defined as:

$$\mathbf{t}_{pq} = \begin{cases} \dfrac{\mathbf{u}_{pq,t}}{\|\mathbf{u}_{pq,t}\|}, & \text{if } \|\mathbf{u}_{pq,t}\| > 0, \\ 0, & \text{otherwise.} \end{cases} \tag{6}$$

In Eq. (6), the instantaneous tangential relative velocity $\mathbf{u}_{pq,t}$ is defined as follows:

$$\mathbf{u}_{pq,t} = \mathbf{u}_{pq} - \mathbf{u}_{pq,n}, \tag{7}$$

where $\mathbf{u}_{pq} = \mathbf{u}_p - \mathbf{u}_q$ is the relative velocity, and $\mathbf{u}_{pq,n} = \left(\mathbf{u}_{pq} \cdot \mathbf{n}_{pq}\right) \mathbf{n}_{pq}$ is the normal component of the relative velocity. $\mathbf{n}_{pq}$ is the normal unit vector given by $\mathbf{n}_{pq} = \left(\mathbf{x}_q - \mathbf{x}_p\right) / \|\mathbf{x}_q - \mathbf{x}_p\|$, with $\mathbf{x}$ being the position vector of the particle center. When $\mathbf{u}_{pq,t}$ is zero, $\mathbf{t}_{pq}$ equals zero, and hence the tangential contact force $\mathbf{f}_{q\to p,t}^c$ is zero (Eq. (5)). This indicates that the contact cannot support any tangential load when the particles are stationary. Thus, the dynamic friction model given by Eq. (5), which is valid for rapid granular flows, is not suitable for fixed beds. To overcome this limitation, a model that accounts for both static and dynamic frictions was implemented in the massively parallel YALES2 code, as described in the next subsection.

2.1. Formulation and implementation of static-dynamic friction

2.1.1. Model formulation

In the static-dynamic friction model, the tangential contact force is composed of elastic (spring) and damping (dashpot) terms and is constrained by the Coulomb limit, as defined by the following equation [36]:

$$\mathbf{f}_{q\to p,t}^c = \begin{cases} \mathbf{f}_{q\to p,t}^*, & \text{if } \|\mathbf{f}_{q\to p,t}^*\| \le \mu_d \|\mathbf{f}_{q\to p,n}^c\|, \\ \mathbf{f}_{q\to p,t}^{\mathrm{CL}}, & \text{if } \|\mathbf{f}_{q\to p,t}^*\| > \mu_d \|\mathbf{f}_{q\to p,n}^c\|, \end{cases} \tag{8}$$

with

$$\mathbf{f}_{q\to p,t}^* = -k_t \boldsymbol{\delta}_{pq,t}^* - \gamma_t \mathbf{u}_{pq,t}, \tag{9}$$

and

$$\mathbf{f}_{q\to p,t}^{\mathrm{CL}} = -k_t \boldsymbol{\delta}_{pq,t}^{\mathrm{CL}} - \gamma_t \mathbf{u}_{pq,t} = \mu_d \|\mathbf{f}_{q\to p,n}^c\| \mathbf{t}_{pq}, \tag{10}$$

where $\mathbf{f}_{q\to p,t}^*$ is the test force, k_t is the tangential spring stiffness, γ_t is the tangential viscous damping coefficient, and $\mathbf{t}_{pq} = \mathbf{f}_{q\to p,t}^* / \|\mathbf{f}_{q\to p,t}^*\|$ is the tangential unit vector. The superscript CL refers to the Coulomb limit. The tangential overlap $\boldsymbol{\delta}_{pq,t}$ depends on the contact history, as it cannot be determined instantaneously but must be accumulated over time and saturated to ensure that the Coulomb limit is never surpassed, as shown in the equation below:

$$\boldsymbol{\delta}_{pq,t} = \begin{cases} \boldsymbol{\delta}_{pq,t}^*, & \text{if } \|\mathbf{f}_{q\to p,t}^*\| \le \mu_d \|\mathbf{f}_{q\to p,n}^c\|, \\ \boldsymbol{\delta}_{pq,t}^{\mathrm{CL}}, & \text{if } \|\mathbf{f}_{q\to p,t}^*\| > \mu_d \|\mathbf{f}_{q\to p,n}^c\|, \end{cases} \tag{11}$$

with

$$\boldsymbol{\delta}_{pq,t}^* = \boldsymbol{\delta}_{pq,t}^{\mathrm{prev}} \cdot \mathbf{H} + \Delta t_p \mathbf{u}_{pq,t}, \tag{12}$$

and

$$\boldsymbol{\delta}_{pq,t}^{\mathrm{CL}} = \frac{1}{k_t}\left(-\mu_d \|\mathbf{f}_{q\to p,n}^c\| \mathbf{t}_{pq} - \gamma_t \mathbf{u}_{pq,t}\right), \tag{13}$$

where Δt_p is the particle time step, and $\boldsymbol{\delta}_{pq,t}^{\mathrm{prev}}$ is the tangential overlap at the previous time step, which is rotated by a matrix $\mathbf{H}$ in order to be situated in the contact plane specified by the new normal unit vector [37]. The rotation matrix $\mathbf{H}$ is defined as:

$$\mathbf{H} = \begin{pmatrix} wb_x^2 + c & wb_x b_y - sb_z & wb_x b_z + sb_y \\ wb_x b_y + sb_z & wb_y^2 + c & wb_y b_z - sb_x \\ wb_x b_z - sb_y & wb_y b_z + sb_x & wb_z^2 + c \end{pmatrix}, \tag{14}$$

where $\mathbf{b}$, c, s, and w are given by:

$$\mathbf{b} = \frac{\mathbf{n}_{pq} \times \mathbf{n}_{pq}^{\mathrm{prev}}}{\left\|\mathbf{n}_{pq} \times \mathbf{n}_{pq}^{\mathrm{prev}}\right\|}, \qquad c = \cos\theta, \qquad s = \sin\theta, \qquad w = 1 - c,$$

with θ defined as:

$$\theta = \arcsin\left(\left\|\mathbf{n}_{pq} \times \mathbf{n}_{pq}^{\mathrm{prev}}\right\|\right),$$

where $\mathbf{n}_{pq}^{\mathrm{prev}}$ is the normal unit vector at the previous time step. The tangential damping parameter γ_t can be formulated as follows:

$$\gamma_t = \frac{-2 \ln e_t}{\sqrt{\pi^2 + \ln^2 e_t}} \sqrt{k_t \frac{2}{7} m_{pq}}, \tag{15}$$

where e_t represents the tangential restitution coefficient. The static-dynamic model (Eq. (8)) has greater computational and memory costs than the Coulomb dynamic model (Eq. (5)). To account for static friction, the tangential overlap of each contact should be stored at each time step.

2.1.2. Model implementation

A multi-level domain decomposition method is employed in YALES2 [18,38]. The grid cells are assembled into cell groups at a first level, and cell groups are distributed over processors at a second level [38]. In the third decomposition level, particles situated in a cell group are gathered in particle groups holding up to 500 particles each [18]. These decomposition levels aim at improving data locality, cache memory accesses, and load balancing.

A ghost particle method is used to treat contacts between particles that are not in the same processor region [18,39]. In this method, a cell halo enclosing each processor region is employed to identify ghost particles [18]. The data of particles located in the cell halo are communicated among the involved processors to calculate the contact force.

Examining all the particles in the domain to determine the contacts with a given particle has a high computational cost, scaling as $\mathcal{O}(N_{tot}^2)$, where N_{tot} is the total number of particles. To deal with this problem, the linked-cell method is used, whose computational cost scales as $\mathcal{O}(N_{tot})$ [35,39–41]. In this technique, a Cartesian grid of size larger than the particle diameter is overlaid on the main grid to identify the potential contact partners of each particle, as shown in Fig. 1. The list of potential contact partners for a given particle is provided by looping over the 8 surrounding Cartesian grid cells plus the one in which the

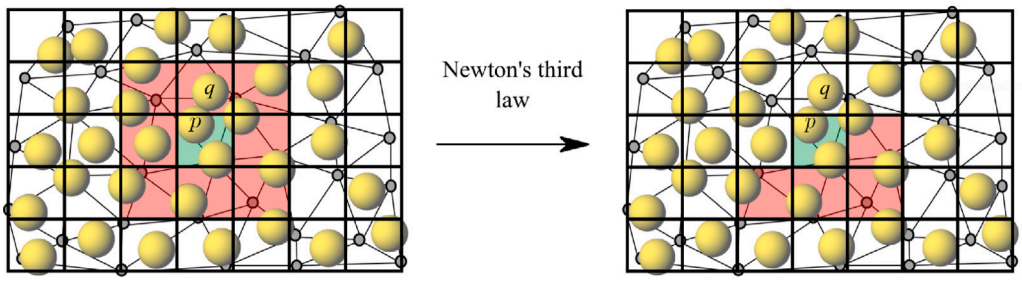

Fig. 1. Linked-cell technique. ◯: nodes of the main grid. ——: overlaid Cartesian grid. The particle of interest is located in the middle cell (▭) and is indicated as p. The particles inside the middle cell or one of the lower neighboring cells (▭) are saved as potential contact partners of particle p.
Source: Adapted from [39].

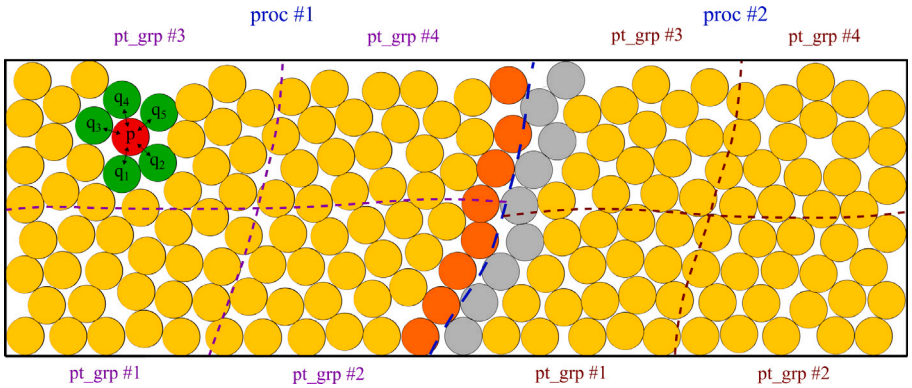

Fig. 2. Particle distribution in a computational domain. — — — : limit between processor domains. – – – : limit between particle groups (pt_grp). ●: ghost particles of processor #2. ◯: ghost particles of processor #1. A particle of interest, p, is in contact with 5 particles.

particle is located (26+1 grid cells in 3D) [39]. However, Newton's third law (action–reaction principle: $\mathbf{f}^c_{p\to q} = -\mathbf{f}^c_{q\to p}$) allows checking only half of these cells (4+1 cells in 2D) [40], and particles situated in these cells are identified as potential contact partners, as illustrated in Fig. 1. During the calculation of the contact force, only the potential contact partners are checked. Once an overlap is detected between a certain particle and one of its potential contact partners, a contact force is computed.

Particles inside a given processor domain are distributed over various particle groups, as illustrated in Fig. 2. In a particle group containing N_g particles, a given particle p has a local index $n_p^{loc} \in [1, N_g]$. This particle has also a unique global index $n_p^{glob} \in [1, N_{tot}]$, where N_{tot} is the total number of particles in the domain. The particle index that was used in the accumulation of the tangential overlap $\boldsymbol{\delta}_{pq,t}$ (Eq. (11)) is the global index because it does not change when the particle moves from one particle group to another or from one processor domain to another. When a particle moves from one CPU to another, the information about its contacts, based on global particle indices, is transferred along with the particle. The particle of interest p in Fig. 2 is in contact with five q particles. Each of these (p, q) contact pairs has a distinct tangential overlap $\boldsymbol{\delta}_{pq,t}$, which must be accumulated over time.

A two-step algorithm for determining the tangential overlap was implemented in YALES2. These two steps are described below.

First step: Insert a new pair in the list of contact pairs and accumulate the tangential overlap. This is achieved by:

(1) Looping over the potential contact partners q of a given particle p at the current time step, or in other words, looping over potential contact pairs. The list of potential contact partners of a given particle is provided by the linked-cell method, as described previously.
(2) Calculating the normal overlap at the current time step ($\delta_{pq,n} = r_p + r_q - \|\mathbf{x}_p - \mathbf{x}_q\|$, where r is the particle radius).
(3) Inserting the pair (p, q) in the list of contact pairs if it is not already there (at the previous time step) and accumulating the tangential overlap $\boldsymbol{\delta}_{pq,t}$, if particles p and q are in contact ($\delta_{pq,n} > 0$).

Second step: Erase an obsolete pair from the list of contact pairs. This is achieved by the following actions:

(1) Looping over particles q that were in contact with a given particle p at the previous time step, or in other words, looping over already existing contact pairs.
(2) Calculating the normal overlap at the current time step.
(3) Erasing the pair (p, q) from the list of contact pairs if the particles p and q are no longer in contact ($\delta_{pq,n} \le 0$).

Each particle situated at a processor boundary has two copies: a real and a ghost. The data of a certain duplicated particle, which are required to compute friction forces, are transmitted from the processor where it is real to the processor where it is ghost.

2.2. Formulation and implementation of Van der Waals force

The Van der Waals force was included in the DEM model by adding an adhesive force term, $\mathbf{F}^{ad}_{q\to p}$, to the particle equation of motion [42]:

$$\mathbf{F}^{ad}_{q\to p} = \frac{A}{6d_p}\frac{1}{\left(2u+u^2\right)^2}\frac{1}{(1+u)^3}\mathbf{n}_{pq}. \tag{16}$$

Here, A denotes the Hamaker constant, $u = \|\mathbf{x}_q - \mathbf{x}_p\|/d_p - 1$ represents the dimensionless separation distance between the two particle surfaces, and $\mathbf{n}_{pq}$ signifies the normal unit vector. When the spheres are nearly touching, the force in Eq. (16) can be written as:

$$\mathbf{F}^{ad}_{q\to p} = \frac{A}{6d_p}\frac{1}{\left(2u_0+u_0^2\right)^2}\frac{1}{\left(1+u_0\right)^3}\mathbf{n}_{pq} \approx \frac{A}{6d_p}\frac{1}{4u_0^2}\mathbf{n}_{pq} = \frac{Ad_p}{24S_0^2}\mathbf{n}_{pq}, \tag{17}$$

where $u_0 = S_0/d_p$ is the minimum dimensionless separation distance, and S_0 is the minimum cutoff distance between the surfaces of the two particles. The Van der Waals interaction diminishes quickly as u

increases. Therefore, to simplify matters, we implemented the Van der Waals force between two particles in the following manner:

$$\mathbf{F}^{ad}_{q\to p} = \begin{cases} \dfrac{Ad_p}{24S_0^2}\mathbf{n}_{pq}, & \text{if } \delta_{pq,n} > 0, \\ 0, & \text{otherwise.} \end{cases} \tag{18}$$

Additionally, we implemented the particle–wall Van der Waals force as [24]:

$$\mathbf{F}^{ad}_{w\to p} = \begin{cases} \dfrac{Ad_p}{12S_0^2}\mathbf{n}_{pw}, & \text{if } \delta_{pw,n} > 0, \\ 0, & \text{otherwise.} \end{cases} \tag{19}$$

2.3. Validation of friction and adhesion models

The static-dynamic friction model was implemented for both interparticle and particle–wall interactions and validated at both micro and macro scales. At the microscale, we found good agreement between the results of our simulations and those obtained using Walton's theoretical model [43] for both interparticle and particle–wall collisions. At the macroscale, we found a close match between the vertical solid stress profile in a silo obtained using the implemented static-dynamic friction model and that determined using Janssen's theoretical model [44], as well as between the mass flow rate of powder exiting a hopper obtained from our simulation and that calculated using Beverloo's empirical correlation [45]. The implementation of the interparticle and particle–wall Van der Waals adhesion forces was qualitatively validated at the microscale by predicting the effects of adhesion on rebound translational and rotational velocities, contact time, and maximum normal overlap [46,47]. The results of the aforementioned validation tests are not presented in this paper since the focus of this study is to investigate the influence of friction and Van der Waals adhesion on fluidization hydrodynamics. Therefore, we only present the prediction of a pressure overshoot in a fluidized bed in the following section.

3. Fluidization and defluidization simulations

3.1. Simulation setup

We conducted fluidization and defluidization CFD-DEM tests to analyze the impact of Van der Waals forces and static wall friction on pressure-drop hysteresis and to gather essential information for guiding the development of macroscopic solid stress models. These simulations, which are similar to those performed by Ye et al. [48], employ the parameters listed in Table 1.

In the initial phase, we conducted particle settling under the influence of gravity ($g_z = -9.81$ m/s^2). The particles used are categorized under Geldart group *A*, with their properties outlined in Table 1. The seeding region was positioned at a distance of d_p from the side walls within the z-range of 4 mm to 6.075 mm. Each cell was seeded with one particle along each dimension ($\Delta x, \Delta y, \Delta z$). Beginning at $t = 0$, we seeded 480 particles at intervals of 0.1 s until $t = 7.4$ s, with the simulation continuing for a total of 9 s. These particles experienced random translation velocities ranging from −0.1 to 0.1 m/s and random rotational velocities between −100 and +100 rad/s at seeding. For this study, we employed a zero rolling friction coefficient. Additionally, Van der Waals forces among particles and between particles and walls were taken into account during the settling process.

Subsequently, we used the formed static bed as the initial state for both fluidization and defluidization tests. Turbulence effects were neglected in these tests. All boundaries were treated as walls for particles. The bottom boundary served as the inlet for gas, and the top boundary functioned as the gas outlet, maintaining a pressure of 1 atm. A no-slip condition was applied to the gas at the sidewalls. In these simulations, we vary the gas mass flow rate at the inlet using a stepwise approach. In this approach, the gas flow rate is maintained at a constant value for a given duration before being instantaneously increased or decreased to a new value for another given period. The mass flow rates are determined by the equation:

$$\dot{W} = \rho_g U_g S_b, \tag{20}$$

where U_g is the superficial gas velocity, and S_b is the cross-sectional area of the bed. Each superficial gas velocity (U_g) was maintained for a duration of $0.7 + H_b^0/U_g$ seconds, where $H_b^0 \approx 3.52$ mm represents the bed height at zero gas velocity. Time averages were computed over the last 0.3 s of each individual time interval during which a specific U_g value was sustained. The Hamaker constant value used in the test cases involving adhesion (refer to Table 1) yields an adhesion force $\mathbf{F}^{ad}_{q\to p}$ equal to $1.18 m_p \mathbf{g}$. As given in Table 1, we used a very small CFL number (0.01) to improve numerical stability because the coupling between the gas and solid phases in YALES2 is explicit.

The drag force can be written as follows:

$$\mathbf{F}^d_p = \frac{1}{\tau^d_r}\left[\mathbf{u}_{g@p} - \mathbf{u}_p\right] m_p, \tag{21}$$

where τ^d_r represents the drag relaxation time, given as:

$$\tau^d_r = \frac{4}{3}\left(\frac{\rho_p d_p^2}{\mu_{g@p} Re_p C_d}\right). \tag{22}$$

Here, C_d stands for the drag coefficient, and Re_p represents the particle Reynolds number, which is written as:

$$Re_p = \frac{d_p \|\mathbf{u}_{g@p} - \mathbf{u}_p\| \rho_{g@p}}{\mu_{g@p}} \alpha_{g@p}. \tag{23}$$

The closure model employed for C_d in our numerical simulations is the one suggested by Gobin et al. [51]:

$$C_d = \begin{cases} C_d^{W\&Y}, & \text{if } \alpha_p \le 0.3, \\ \min(C_d^E, C_d^{W\&Y}), & \text{else.} \end{cases} \tag{24}$$

Here, C_d^E represents the drag coefficient according to Ergun [52]:

$$C_d^E = \frac{1}{\alpha_{g@p}}\left[\frac{7}{3} + \frac{200}{Re_p}\left(1 - \alpha_{g@p}\right)\right], \tag{25}$$

and $C_d^{W\&Y}$ is the Wen and Yu drag coefficient [53] defined as:

$$C_d^{W\&Y} = \begin{cases} 0.44\alpha_{g@p}^{-2.7}, & \text{if } Re_p \ge 1000, \\ \dfrac{24}{Re_p}\alpha_{g@p}^{-2.7}\left(1 + 0.15 Re_p^{0.687}\right), & \text{else,} \end{cases} \tag{26}$$

where $\alpha_{g@p}$ is the volume fraction of the gas interpolated at the position of the particle. This drag model ensures a continuous transition between the Ergun and Wen & Yu correlations and gives satisfactory predictions compared to direct numerical simulation (DNS) data [51, 54].

3.2. Prediction of the pressure-drop hysteresis and of the homogeneous fluidization regime

The time-averaged bed pressure drop was calculated using the formula:

$$\overline{\Delta P} = \frac{\sum_{k=1}^{N_r} \Delta P_k \Delta t_{g,k}}{\sum_{k=1}^{N_r} \Delta t_{g,k}}. \tag{27}$$

Here, Δt_g represents the gas time step, ΔP is the gas pressure drop between the inlet and 6.5 mm above the inlet, and N_r is the total number of gas time steps in the 0.3 s interval. Then, the normalized time-averaged bed pressure drop was determined as $\overline{\Delta P}/\Delta P_{eq}$, where ΔP_{eq} represents the pressure drop equivalent to the weight of the particles, which was computed as:

$$\Delta P_{eq} = \frac{m_b g}{S_b} = \frac{\pi d_p^3}{6}\frac{N_{tot}\rho_p g}{S_b} = 32.4 \text{ Pa}. \tag{28}$$

In this equation, m_b represents the mass of the particle bed, and N_{tot} represents the number of all the particles. Fig. 3 illustrates the

Table 1
Parameters for the fluidization and defluidization simulations.

Particle properties		*Interparticle and particle–wall collisions*	
Diameter, d_p	75 μm	Normal spring stiffness, k_n	7 N/m
Density, ρ_p	1495 kg/m^3	Normal restitution coefficient, e_n	0.9
		Tangential spring stiffness, k_t	2 N/m
Cuboid geometry		Tangential restitution coefficient, e_t	0.9
Width (x-direction), W	$40d_p$	Dynamic friction coefficient, μ_d	0.2
Thickness (y-direction), T	$16d_p$	Maximum normal overlap, δ_n^{max}	$0.1d_p$
Height (z-direction), H	$160d_p$		
		Gas properties	
Hexahedral mesh		Density, ρ_g	1.1979 kg/m^3
Number of cells in the x-direction, N_c^x	12	Viscosity, μ_g	1.8×10^{-5} Pa s
Number of cells in the y-direction, N_c^y	5		
Number of cells in the z-direction, N_c^z	48	*Advancement of gas*	
		Time integration scheme	TFV4A [49]
Particle loading		Spatial integration scheme	4th-order centered
Number of particles, N_{tot}	36,000	Courant number, CFL	0.01
Time advancement of particles		*Gas–particle interaction*	
Numerical scheme	Groot–Warren [50]	Drag model	Gobin et al. [51]
Particle CFL number, CFL_s	1.5		
Contact CFL number, CFL_s^c	0.05	*Interparticle and particle–wall adhesion*	
Number of sub-steps within the collision time, n_c	15	Minimum cutoff distance, S_0	4×10^{-10} m
		Hamaker constant, A	1.96×10^{-22} J

fluidization and defluidization pressure-drop curves for tests with and without adhesion effects (interparticle and particle–wall Van der Waals adhesion). The figure displays an overshoot in the bed pressure drop during fluidization, which is attributed to static wall friction in the case without adhesion. It also shows that the overshoot intensity increases when adhesion is present. Moreover, there is a hysteresis in pressure drop between the decreasing and increasing velocity path curves (defluidization and fluidization cycles, respectively).

The pressure drop in the static bed state can be approximated using the Ergun [52] correlation:

$$\frac{\Delta P}{H_b} = 1.75\rho_g \frac{\left(1-\alpha_g\right)\mathrm{U}_g^2}{\alpha_g^3 \varepsilon_p d_p} + 150\mu_g \frac{\left(1-\alpha_g\right)^2 \mathrm{U}_g}{\alpha_g^3 \left(\varepsilon_p d_p\right)^2}, \tag{29}$$

where H_b is the bed height, α_g is the voidage of the bed, and ε_p is the particle sphericity. As shown in Fig. 3, there is a good match between the Ergun equation and the simulation results.

A fluidization simulation that excluded both adhesion and particle–wall friction showed no overshoot. Another fluidization simulation, which accounted for interparticle adhesion but excluded particle–wall adhesion, demonstrated a smaller overshoot area compared to the simulation that considered both interparticle and particle–wall adhesion. The data from these two simulations are not presented here.

In this study, we used a small simulation domain due to the high computational cost. Increasing the domain size would reduce the contribution of boundary interactions (wall friction and adhesion) to the overshoot [13,15].

In our simulations, where all cells have the same volume, the time-spatial averaged solid volume fraction was computed as follows:

$$\overline{\langle\alpha_p\rangle} = \frac{\sum_{k=1}^{N_r}\langle\alpha_p\rangle_k \Delta t_{g,k}}{\sum_{k=1}^{N_r}\Delta t_{g,k}} = \frac{v_p}{v_{sa}} \frac{\sum_{k=1}^{N_r} n_{sa,k}\Delta t_{g,k}}{\sum_{k=1}^{N_r}\Delta t_{g,k}}, \tag{30}$$

where v_p is the volume of one particle ($\pi d_p^3/6$), v_{sa} is the total volume below a designated height H_{sa} where spatial averaging was performed, and n_{sa} is the total number of particles situated below the height H_{sa}. This height is set at $H_{sa} = 14\Delta z = 3.5$ mm, which is approximately equal to the bed height when the gas velocity is zero. The bed voidage was then determined as follows: $\overline{\langle\alpha_g\rangle} = 1 - \overline{\langle\alpha_p\rangle}$.

The evolution of bed voidage during defluidization and fluidization cycles is plotted in Fig. 4. In the fluidization branch, the bed voidage remains stable at around 0.38 until reaching the minimum fluidization velocity (U_{mf} = 3.32 mm/s), after which it begins to increase. The decreasing path curves do not return to the voidage of the settled bed, aligning with observations from experiments by Affleck et al. [22],

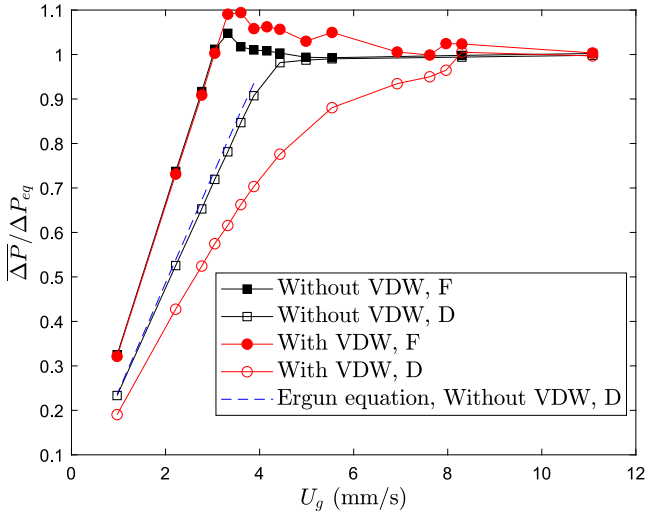

Fig. 3. Normalized time-averaged overall bed pressure drop during fluidization and defluidization cycles without and with Van der Waals (VDW) adhesion. *F* represents a fluidization branch, and *D* represents a defluidization branch.

particularly when the particle bed is tapped before fluidization. Additionally, defluidization curves differ between tests with and without adhesion, with adhesion resulting in a higher voidage for the static bed due to hindered particle movement, consistent with findings in the fixed bed simulations by Mihajlovic et al. [47].

The minimum fluidization velocity calculated using the correlation proposed by Abrahamsen and Geldart [55], which is expressed as:

$$U_{mf} = 9 \times 10^{-4} \left(g\left[\rho_p - \rho_g\right]\right)^{0.934} \frac{d_p^{1.8}}{\mu_g^{0.87}\rho_g^{0.066}}, \tag{31}$$

is approximately 3.5 mm/s. The simulation value of 3.32 mm/s is only about 5% lower than this estimate, indicating a very close agreement.

The time-spatial averaged coordination number was computed in the following manner:

$$\overline{\langle CN\rangle} = \frac{\sum_{k=1}^{N_r}\langle\alpha_p\rangle_k\langle CN\rangle_k \Delta t_{g,k}}{\sum_{k=1}^{N_r}\langle\alpha_p\rangle_k \Delta t_{g,k}} = \frac{\sum_{k=1}^{N_r} n_{sa,k}\langle CN\rangle_k \Delta t_{g,k}}{\sum_{k=1}^{N_r} n_{sa,k}\Delta t_{g,k}}$$

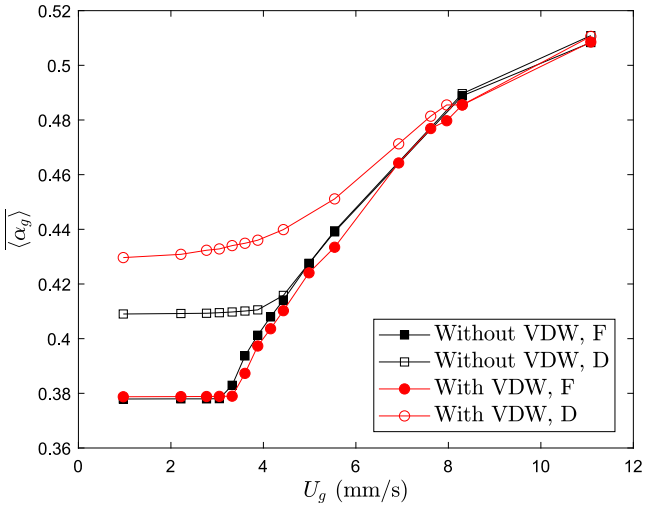

Fig. 4. Bed voidage profiles during defluidization (D) and fluidization (F) cycles without and with Van der Waals (VDW) adhesion.

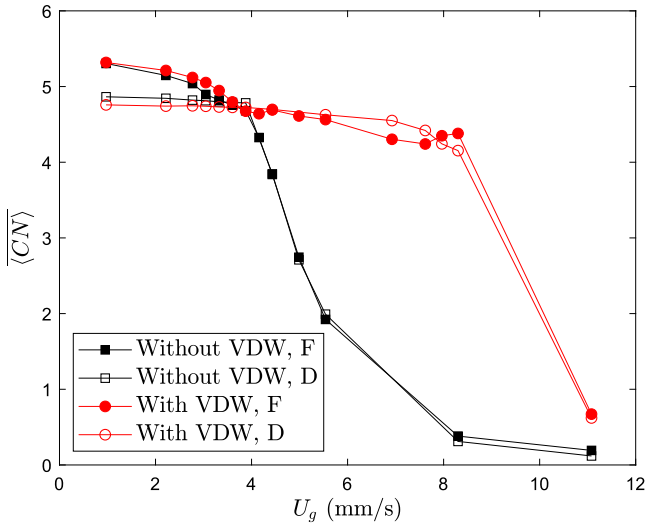

Fig. 5. Evolution of the coordination number during defluidization (D) and fluidization (F) cycles, without and with Van der Waals (VDW) adhesion.

$$= \frac{\sum_{k=1}^{N_r} \left(\sum_{i=1}^{n_{sa,k}} CN_i \right) \Delta t_{g,k}}{\sum_{k=1}^{N_r} n_{sa,k} \Delta t_{g,k}}. \tag{32}$$

The evolution of the coordination number during defluidization and fluidization cycles is presented in Fig. 5. A hysteresis is observed for the average coordination number predictions between the decreasing and increasing gas velocity paths (below U_{mf}). In the absence of adhesion, the average coordination number decreases rapidly to nearly zero with the increase in superficial gas velocity (above U_{mf}) for both the defluidization and fluidization cycles. In contrast, in the presence of Van der Waals adhesion, the coordination number slowly decreases with the increase in superficial gas velocity (up to $U_g = 8.3$ mm/s). In the fluidization and defluidization branches with adhesion, increasing the superficial gas velocity from 4.43 mm/s to 6.93 mm/s, for example, does not significantly decrease the coordination number despite an increase in the voidage (see Fig. 4). This is a characteristic of the homogeneous fluidization regime. Therefore, the coordination number variations in Fig. 5 reveal that predicting the homogeneous regime between the minimum fluidization and minimum bubbling velocities requires accounting for the Van der Waals adhesion. Some tests (not shown here) have demonstrated that suppressing Van der Waals adhesion between particles and walls does not alter the homogeneous fluidization regime and the overall coordination number trend.

For fluidization to occur, the forces exerted by the gas on the particles must overcome the weight of the particles. However, this is true only if particle–wall interactions (friction and adhesion), which resist the movement of all particles, are neglected. In the presence of these forces, the gas must exert an additional force beyond the bed weight to fluidize the particles. This results in an overshoot region where the pressure drop exceeds the value corresponding to the particles' weight. During defluidization, particle–wall friction opposes the downward movement of the particles, preventing the bed from becoming as dense as the one formed after filling. In addition, the internal stresses developed during filling are relieved after fluidization, so the bed does not return to its initial voidage and fewer contacts are formed after defluidization (see the differences in bed voidage and coordination number for $U_g < U_{mf}$ between fluidization and defluidization in Figs. 4 and 5). This difference results in pressure drop hysteresis between the defluidization and fluidization cycles.

Additionally, the contact fabric tensor was computed as follows [56]:

$$R_{ij} = \frac{1}{N_{tot}} \sum_{k=1}^{N_{tot}} \sum_{c=1}^{c_k} n_{k,i}^{c} n_{k,j}^{c}, \tag{33}$$

where N_{tot} represents the number of particles in the bed ($N_{tot} = 36{,}000$ in our case), c_k denotes the count of contacts on particle k, and $\mathbf{n}_k^c$ indicates the unit branch vector that originates from the center of particle k and points towards a contact point c. The trace of this fabric tensor is equal to the average coordination number of all the particles. The fabric tensor, R_{ij}, is symmetric. The fabric component R_{zz} at a particular gas time step Δt_g was calculated by averaging over the particle time steps as follows:

$$R_{zz} = \frac{1}{N_{tot}} \left(\frac{\sum_{j=1}^{N_{st}} \left(n_{1,z}^{1} n_{1,z}^{1} + \cdots + n_{1,z}^{c_1} n_{1,z}^{c_1} \right)_j \Delta t_{p,j}}{\sum_{j=1}^{N_{st}} \Delta t_{p,j}} + \cdots \cdots + \frac{\sum_{j=1}^{N_{st}} \left(n_{N_{tot},z}^{1} n_{N_{tot},z}^{1} + \cdots + n_{N_{tot},z}^{c_{N_{tot}}} n_{N_{tot},z}^{c_{N_{tot}}} \right)_j \Delta t_{p,j}}{\sum_{j=1}^{N_{st}} \Delta t_{p,j}} \right). \tag{34}$$

Here, Δt_p is the particle time step, and N_{st} is the number of sub-steps (particle time steps) in a given gas time step. The time-averaged R_{zz} was then computed as:

$$\overline{R_{zz}} = \frac{\sum_{k=1}^{N_r} R_{zz,k} \Delta t_{g,k}}{\sum_{k=1}^{N_r} \Delta t_{g,k}}. \tag{35}$$

The other fabric tensor components were determined similarly to how $\overline{R_{zz}}$ was calculated.

Fig. 6 shows the diagonal components of the fabric tensor as a function of the superficial gas velocity during defluidization and fluidization cycles, without and with adhesion. The R_{zz} component of the fabric tensor indicates the degree of alignment of contacts within the particle bed (orientation of the unit branch vector) along the z-axis. As observed in Fig. 6, the fabric component $\overline{R}_{zz}$ exhibits higher values in the fixed bed state compared to the fabric components $\overline{R}_{xx}$ and $\overline{R}_{yy}$, indicating that more contacts are oriented in the z direction than in the x and y directions. In the fixed bed state, the variation in these diagonal components with the gas velocity is relatively small, indicating that the contact orientations in the x, y, and z directions remain nearly unchanged. At high gas velocities, the fabric diagonal components decrease significantly and reach very small values as contacts are lost. In the presence of adhesion, the fabric diagonal components maintain high values at higher gas velocities compared to the case without adhesion. This implies that adhesion inhibits changes in contact orientations and the disintegration of the contact network.

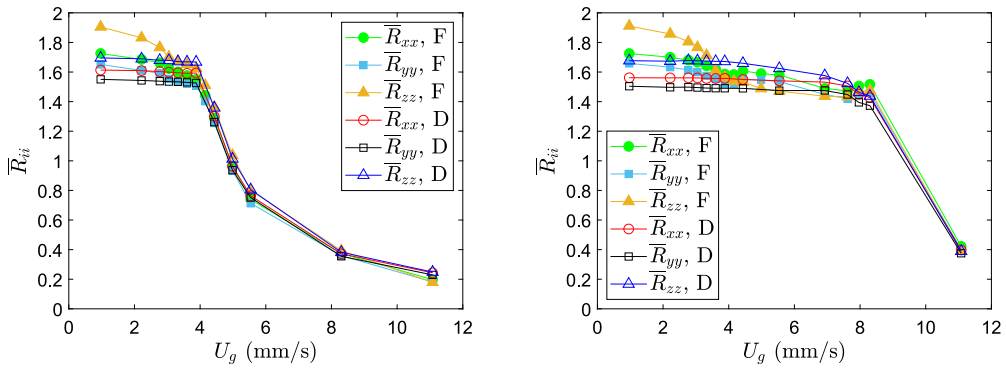

Fig. 6. Variation of the time-averaged diagonal components of the fabric tensor with the superficial gas velocity during defluidization (D) and fluidization (F) cycles for test cases: (a) without Van der Waals adhesion, and (b) with Van der Waals adhesion.

3.3. Spatial distribution of coordination number and particle velocity

Fig. 7 shows the solid patterns during the fluidization cycle without adhesion. In Fig. 7(a), the distribution of the number of contacts per particle (CN) in the fixed bed (at $U_g = 0.97$ mm/s) is homogeneous, with an average value of nearly 5. Increasing the gas velocity to 5.54 mm/s causes the bed to expand, leading to a decrease in the coordination number (see Fig. 7(b)). A further increase in gas velocity to 11.08 mm/s results in significant bed expansion, bubble formation, and a substantial decrease in the coordination number, which drops to zero for the majority of the particles (see Fig. 7(c)). Fig. 7(d) shows that the particle velocity is high around the bubbles, particularly in the wake region.

Fig. 8 shows a comparison of the number of contacts per particle at a superficial gas velocity of 5.54 mm/s between cases with and without adhesion. The presence of adhesion prevents the destruction of the contact network, in contrast to the case without adhesion, where contacts are lost and the coordination number decreases markedly.

With adhesion, the particles undergo a homogeneous expansion phase (see Fig. 8(a)) before the onset of bubbling. During this phase, the bed expands uniformly, maintaining a relatively stable structure and largely preserving the interparticle contacts. On the other hand, without adhesion, particles do not experience a homogeneous expansion phase. Instead, the drag force exerted by the gas on the particles breaks the interparticle contacts (see Fig. 8(b)), allowing bubbles to form.

3.4. Variation of solid pressure and particle–wall shear stress

The macroscopic collisional stress tensor in an averaging volume V can be expressed as [29,56,57]:

$$\sigma_{ij} = -\frac{1}{V}\sum_{k=1}^{n_s}\sum_{c=1}^{c_k} l_{k,i}^{c} f_{k,j}^{c}, \tag{36}$$

where n_s is the number of particles whose centers lie within the volume V, c_k is the number of contacts on particle k, $\boldsymbol{l}_k^c$ is the branch vector from the center of particle k to a contact point c, and $\mathbf{f}_k^c$ is the contact force acting on particle k. For a particle p in contact with a particle q at a point c, the branch vector $\boldsymbol{l}_p^c$ is given by:

$$\boldsymbol{l}_p^c = \left(\frac{d_p}{2} - \frac{\delta_{pq,n}}{2}\right)\mathbf{n}_{pq}. \tag{37}$$

The computational domain was divided into 32 slices, each with a thickness of $\Delta z = 5d_p$, as illustrated in Fig. 9. The collisional stress was calculated for each slice.

The time-averaged σ_{zz}, for instance, was calculated as follows:

$$\overline{\sigma_{zz}} = \frac{\sum_{k=1}^{N_r}\sigma_{zz,k}\Delta t_{g,k}}{\sum_{k=1}^{N_r}\Delta t_{g,k}}, \tag{38}$$

where $\sigma_{zz,k}$ is the collisional stress zz-component at a given gas time step $\Delta t_{g,k}$, calculated by averaging over the particle time steps as follows:

$$\sigma_{zz} = -\frac{1}{V}\left(\frac{\sum_{j=1}^{N_{st}}(\overbrace{l_{1,z}^{1}f_{1,z}^{1} + \cdots + l_{1,z}^{c_1}f_{1,z}^{c_1}}^{\text{particle 1}})_j \Delta t_{p,j}}{\sum_{j=1}^{N_{st}}\Delta t_{p,j}} + \cdots\cdots + \frac{\sum_{j=1}^{N_{st}}(\overbrace{l_{n_s,z}^{1}f_{n_s,z}^{1} + \cdots + l_{n_s,z}^{c_{n_s}}f_{n_s,z}^{c_{n_s}}}^{\text{particle } n_s})_j \Delta t_{p,j}}{\sum_{j=1}^{N_{st}}\Delta t_{p,j}}\right). \tag{39}$$

where n_s is the number of particles located inside a given slice of volume V. The contribution of particle–wall interactions was not included in the computation of the stress given by Eq. (39). The time-averaged repulsive solid pressure was then determined as:

$$\overline{P_p^r} = \frac{1}{3}\left(\overline{\sigma_{xx}} + \overline{\sigma_{yy}} + \overline{\sigma_{zz}}\right). \tag{40}$$

The time-averaged adhesive solid pressure $\overline{P_p^a}$ was computed similarly to the repulsive solid pressure $\overline{P_p^r}$, but using the Van der Waals force instead of the collision force. The effective solid pressure is the sum of the repulsive and adhesive solid pressures:

$$\overline{P_p^e} = \overline{P_p^r} + \overline{P_p^a}. \tag{41}$$

Fig. 10 shows the variation of repulsive solid pressure with depth for different superficial gas velocities, with each curve belonging to either the fluidization or defluidization branch. These data are from a test case without adhesion. As observed, at the lowest gas velocity of 0.97 mm/s, where the bed is fixed, the repulsive solid pressure increases with depth. Additionally, the repulsive solid pressure decreases as the gas velocity increases because the contact network between the particles is disrupted. At a gas velocity of 4.43 mm/s, the repulsive solid pressure approaches zero due to the expansion of the bed. Furthermore, there is a noticeable difference in the repulsive solid pressure values between the defluidization and fluidization curves, for example, at gas velocities of 0.97, 2.22, and 2.77 mm/s, where the defluidization curves exhibit lower repulsive pressure values. This is consistent with the higher voidage values observed at these velocities during defluidization compared to fluidization. In the defluidization cycle, a reduction in gas velocity from 3.88 to 3.05 mm/s leads to an increase in repulsive pressure due to the compression of the bed. This results in higher repulsive pressures during defluidization compared to fluidization, specifically in the lower regions of the bed. The transition from higher repulsive pressures during defluidization in comparison with fluidization to the

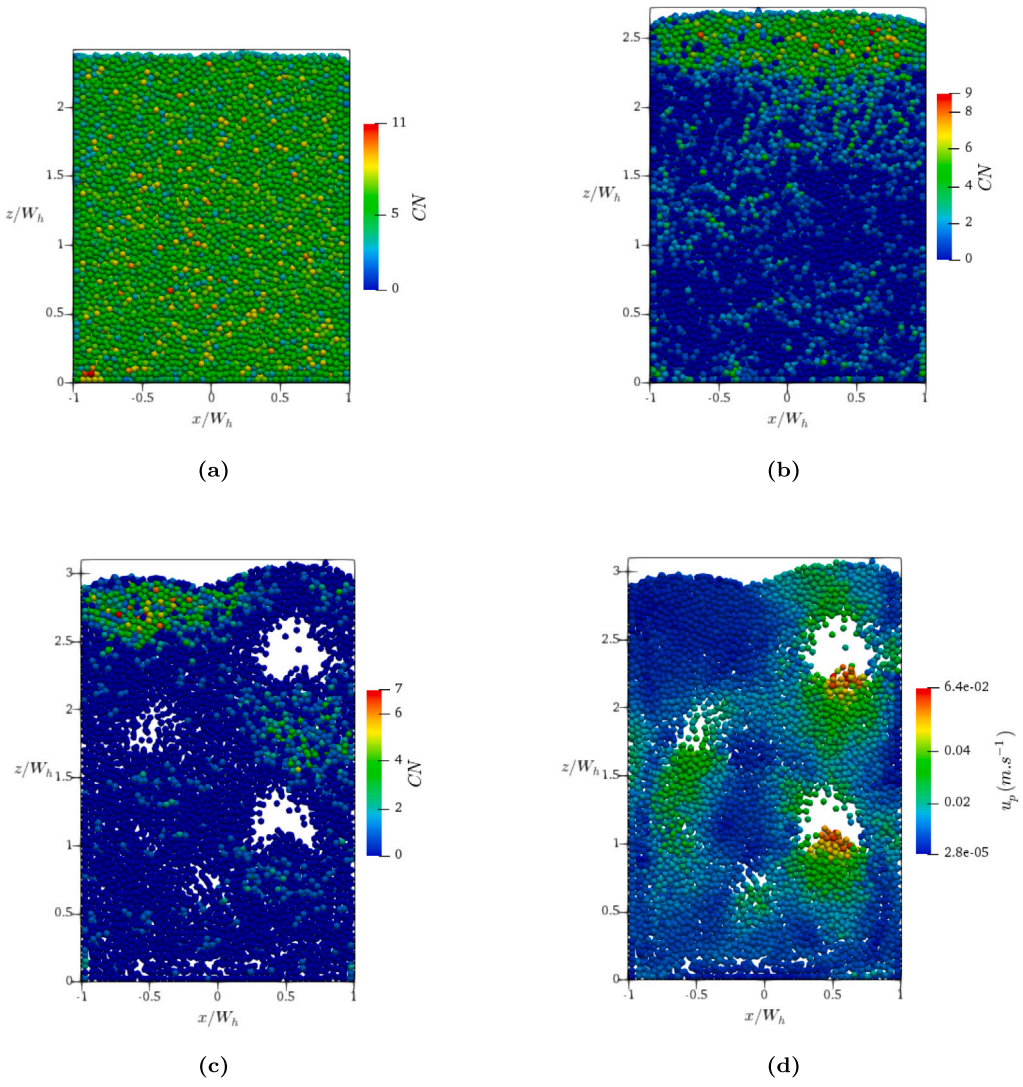

Fig. 7. Solid pattern snapshots for the fluidization branch of the test case without adhesion: (a–c) Coordination number at U_g = 0.97, 5.54, and 11.08 mm/s, respectively; (d) Particle velocity at U_g = 11.08 mm/s. W_h represents half the width of the cuboid.

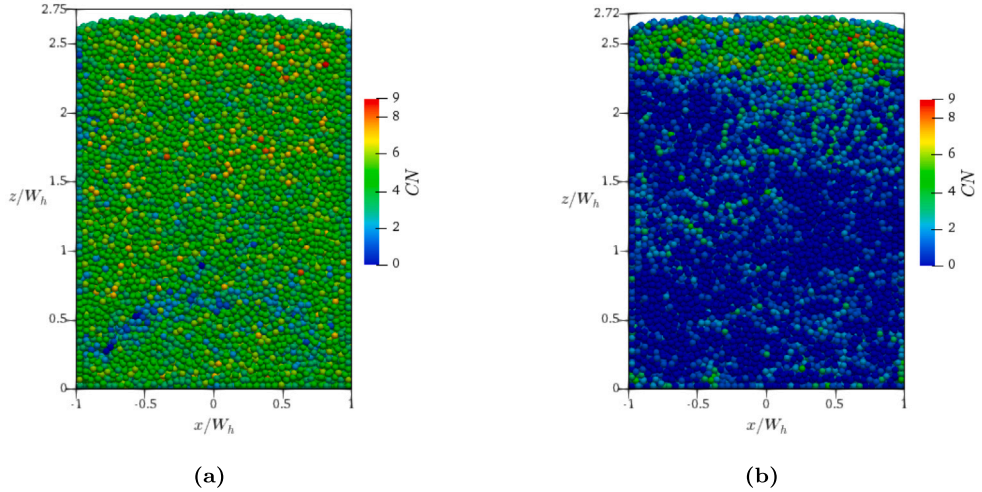

Fig. 8. Comparison of number of contacts per particle at a superficial gas velocity of 5.54 mm/s: (a) with vs. (b) without Van der Waals adhesion.

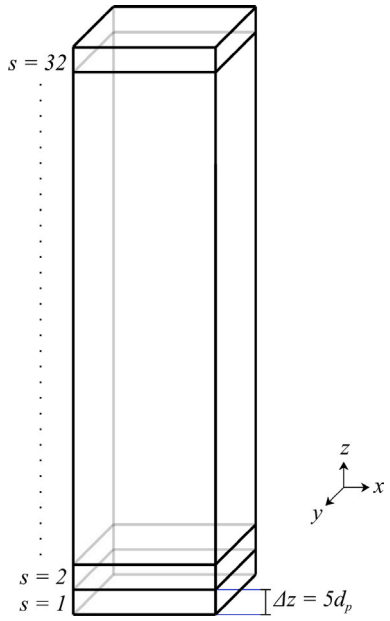

Fig. 9. Division of the cuboid into slices. s denotes the slice number. Each slice has a thickness $\Delta z = 5d_p$.

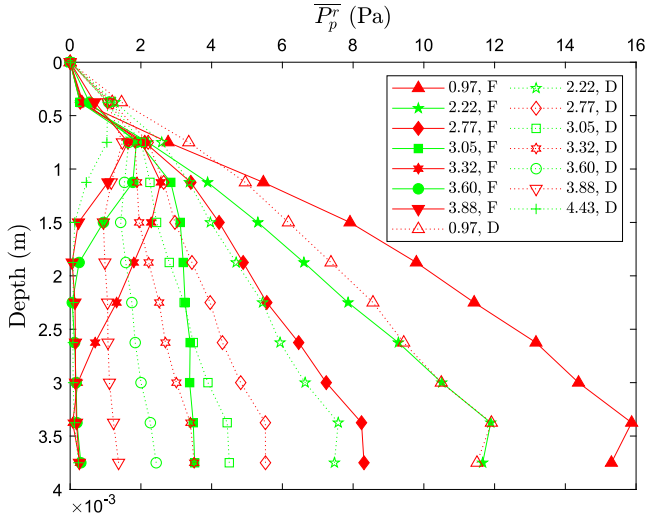

Fig. 10. Variation of time-averaged repulsive particle pressure with depth during defluidization (D) and fluidization (F) cycles without Van der Waals adhesion. The numbers in the legends of this figure and Figs. 11, 12, and 13 are the superficial gas velocity values in mm/s.

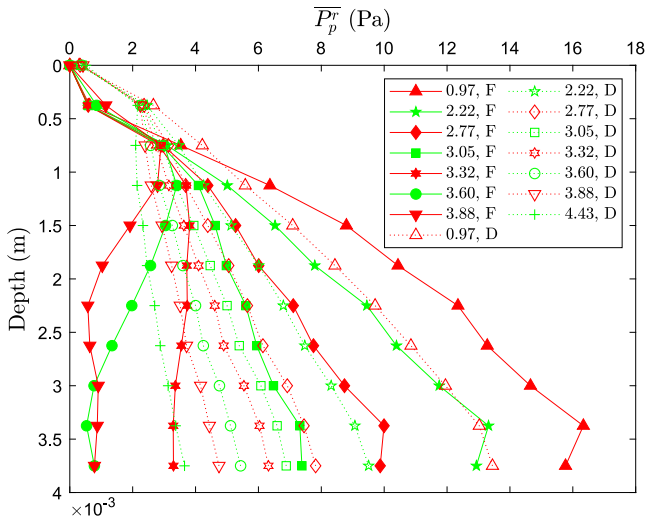

Fig. 11. Variation of time-averaged repulsive particle pressure with depth during defluidization (D) and fluidization (F) cycles with Van der Waals adhesion.

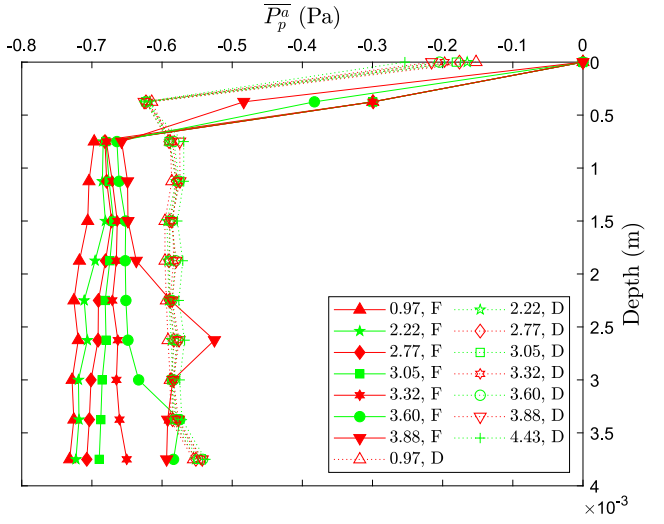

Fig. 12. Variation of time-averaged adhesive particle pressure with depth during defluidization (D) and fluidization (F) cycles.

opposite occurs at a gas velocity of 3.05 mm/s, at which the bed voidage starts to increase in the fluidization branch (refer to Fig. 4).

Figs. 11, 12, and 13 illustrate the repulsive, adhesive, and effective solid pressures during defluidization and fluidization cycles with Van der Waals adhesion. In Fig. 11, within the fluidization branch at a velocity of 3.05 mm/s, for example, the repulsive pressure is higher compared to the case without adhesion (see Fig. 10). This increase is due to adhesion inhibiting the expansion of the bed. The shift from higher repulsive pressures during defluidization compared to fluidization to the opposite happens at a gas velocity of 3.32 mm/s, where the bed voidage begins to rise in the fluidization branch (see Fig. 4).

In Fig. 12, we observe that the adhesive solid pressure during defluidization generally exhibits a lower magnitude compared to that during fluidization. This is consistent with the higher bed voidage and lower coordination number during defluidization compared to fluidization because the Van der Waals force is applied at contact. Additionally, as the superficial gas velocity increases along the fluidization branch, the magnitude of adhesive pressure decreases due to the declining coordination number. Unlike repulsive pressure, adhesive pressure does not vary significantly with depth due to the uniform coordination number distribution within the bed and the constant magnitude of the applied Van der Waals forces.

In Fig. 13, we note that the effective pressure values are lower than the repulsive pressure values indicated in Fig. 11 due to the negative adhesion contribution, as per Eq. (41).

The particle–wall contact forces were calculated in each slice. For instance, the z-component of the particle–wall contact force at a particular gas time step was determined by averaging over the particle time steps as follows:

$$f^a_{w\to p,z} = \frac{\sum_{j=1}^{N_{st}} f_{w\to p,z}|_j \Delta t_{p,j}}{\sum_{j=1}^{N_{st}} \Delta t_{p,j}} = \frac{\sum_{j=1}^{N_{st}} f_{w\to p,z}|_j \Delta t_{p,j}}{\Delta t_g}, \tag{42}$$

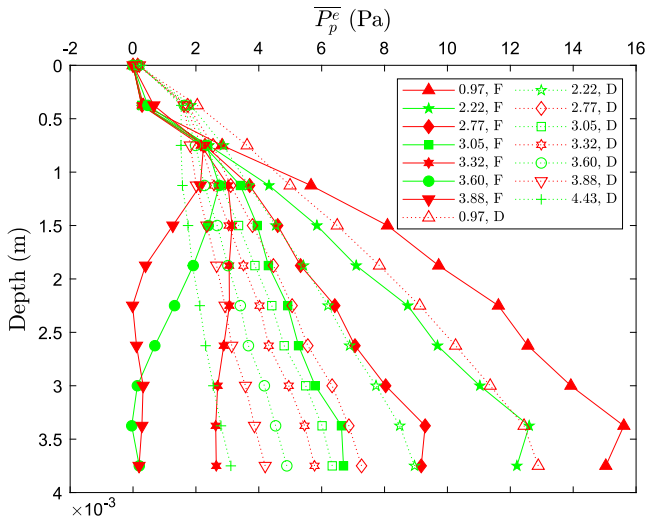

Fig. 13. Variation of time-averaged effective particle pressure with depth during defluidization (D) and fluidization (F) cycles with Van der Waals adhesion.

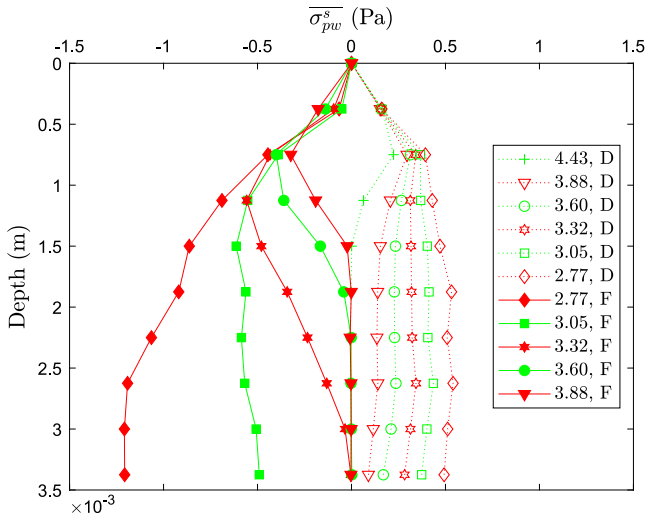

Fig. 14. Variation of time-averaged particle–wall shear stress with depth during defluidization (D) and fluidization (F) cycles without Van der Waals adhesion. The numbers in the legend are the superficial gas velocity values in mm/s.

where $f_{w\to p,z}|_j$ represents the z-component of the contact force applied by all walls w to particle p at the particle time step $\Delta t_{p,j}$, and Δt_g is the gas time step. When adhesion is present, $\mathbf{f}_{w\to p}$ is the sum of repulsive contact force (modeled by spring–dashpot systems in both the tangential and normal directions) and adhesive contact force (Van der Waals force in the normal direction). The sum of the contact force over all particles with centers located within slice s was determined as follows:

$$F^s_{w\to p,z} = \sum_{n_s} f^a_{w\to p,z}, \tag{43}$$

where n_s denotes the number of particles in the slice s at Δt_g. The time average of $F^s_{w\to p,z}$ was then calculated as follows:

$$\overline{F}^s_{w\to p,z} = \frac{\sum_{k=1}^{N_r} F^s_{w\to p,z}|_k \Delta t_{g,k}}{\sum_{k=1}^{N_r} \Delta t_{g,k}}, \tag{44}$$

where N_r is the total number of gas time steps in the averaging time interval. To obtain the time-averaged particle–wall shear stress $\overline{\sigma_{pw}^s}$, we divided $\overline{F}^s_{w\to p,z}$ by the wall surface area S_w, which is given by:

$$S_w = 2W\Delta z + 2T\Delta z = 560 d_p^2. \tag{45}$$

Here, $\Delta z = 5d_p$ represents the thickness of the slice s. W and T refer to the width and thickness of the cuboid, as specified in Table 1.

Fig. 14 depicts the variation of time-averaged particle–wall shear stress with depth during defluidization (D) and fluidization (F) cycles in the absence of Van der Waals adhesion. In defluidization, the shear stress is positive, whereas it is negative during fluidization. During the defluidization cycle, as gas velocity decreases, the wall friction opposes the downward movement of particles, resulting in a positive shear stress (in the positive z direction). Conversely, during the fluidization cycle, as gas velocity increases, wall friction counteracts the upward movement of particles, leading to a negative shear stress (in the negative z direction). Loezos et al. [58] employed a positive sign for the particle–wall friction term in a particle force balance model during defluidization, while a negative sign was used during fluidization. Furthermore, Fig. 14 shows that as the superficial gas velocity rises, the magnitude of the particle–wall shear stress diminishes. This occurs because the increase in gas velocity leads to a reduction in the number of contacts, particularly between particles near the walls.

4. Computation of the coordination number source term

In our previous study [59], we proposed an adhesive pressure model based on the coordination number within the Eulerian–Eulerian framework. This model successfully predicted an overshoot in the bed pressure drop; however, it could not predict the hysteresis in the pressure drop due to the lack of a model for the coordination number evolution. To determine this evolution at the macro-scale, it is essential to propose a transport equation for the coordination number. The first step in this process is to measure the source term of this transport equation. This measurement is crucial for developing and validating an expression for the source term, which can then be utilized in two-fluid simulations. In this section, we compute the coordination number source term from our CFD-DEM simulations using two methods: the direct Lagrangian method and the mesoscopic Eulerian method, which are detailed in the following subsections.

4.1. Direct Lagrangian method

The Lagrangian equation of the coordination number CN following a given particle can be written as:

$$\frac{dCN}{dt} = S_{CN}, \tag{46}$$

where d/dt is the time derivative along the particle trajectory, and S_{CN} is a source term. The corresponding Eulerian equation can be written for uniform particle mass as follows:

$$\frac{D}{Dt}\left(n_p\langle CN\rangle\right) = n_p\left\langle\frac{dCN}{dt}\right\rangle, \tag{47}$$

where n_p denotes the particle number density, and $\langle CN\rangle$ stands for the ensemble average of the coordination number. The term on the left-hand side of Eq. (47) can be expressed as:

$$\frac{D}{Dt}\left(n_p\langle CN\rangle\right) = \frac{\partial}{\partial t}\left(n_p\langle CN\rangle\right) + \frac{\partial}{\partial x_i}\left(n_p U_{p,i}\langle CN\rangle\right) + \frac{\partial}{\partial x_i}\left(n_p\langle u'_{p,i}CN\rangle\right). \tag{48}$$

Here, $U_{p,i} = \langle u_{p,i}\rangle$ represents the average particle velocity, and $u'_{p,i}$ denotes the uncorrelated random particle velocity. The term on the right-hand side of Eq. (47) represents the source term and can be calculated directly from the Lagrangian simulation:

$$n_p\langle S_{CN}\rangle = n_p\left\langle\frac{dCN}{dt}\right\rangle = \frac{1}{V_c}\sum_{k=1}^{N_p^c}\frac{dCN_k}{dt}, \tag{49}$$

where V_c stands for the volume of a given cell, and N_p^c refers to the number of particles whose centers are inside this cell. With the direct Lagrangian method, Eq. (49) is used to compute the source term from CFD-DEM simulations. The time derivative in Eq. (49) was calculated

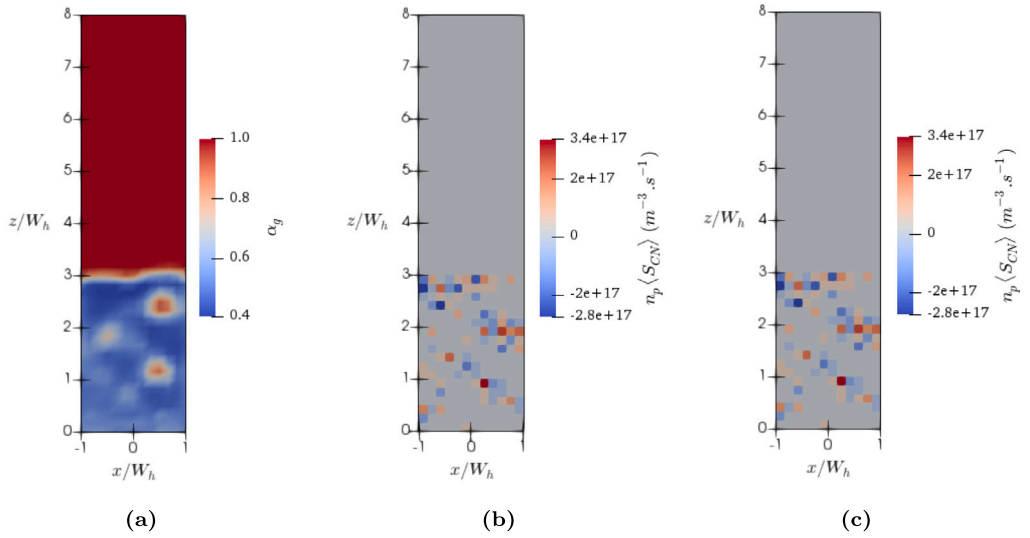

Fig. 15. Computation of the coordination number source term at U_g = 11.08 mm/s: instantaneous distributions of (a) gas volume fraction, (b) coordination number source term computed using the direct Lagrangian method, and (c) coordination number source term computed using the mesoscopic Eulerian method. W_h represents half the width of the cuboid.

for a specific particle k with a backward difference:

$$\left.\frac{dCN_k}{dt}\right|_n = \frac{CN_k|_n - CN_k|_{n-1}}{\Delta t_g}, \tag{50}$$

where n and $n-1$ represent the current and previous states, respectively, and Δt_g stands for the gas time step.

4.2. Mesoscopic Eulerian method

We assume that the last term in Eq. (48) is negligible. Then, we can write the following:

$$\frac{D}{Dt}\left(n_p\langle CN\rangle\right) = \frac{\partial}{\partial t}\left(n_p\langle CN\rangle\right) + \frac{\partial}{\partial x_i}\left(n_p U_{p,i}\langle CN\rangle\right) = n_p\langle S_{CN}\rangle. \tag{51}$$

In this equation, it is assumed that the mean coordination number $\langle CN\rangle$ is convected with the local average velocity (correlated mesoscopic velocity) of the particles $U_{p,i}$, and that no diffusive transport takes place. Using Eq. (51), the source term can be expressed as:

$$n_p\langle S_{CN}\rangle = \frac{1}{v_p}\left[\frac{\partial}{\partial t}\left(\alpha_p\langle CN\rangle\right) + \frac{\partial}{\partial x_i}\left(\alpha_p U_{p,i}\langle CN\rangle\right)\right], \tag{52}$$

where $v_p = \pi d_p^3/6$ denotes the volume of one particle. The partial derivatives in Eq. (52) can be computed from the calculated Eulerian variables. The mean coordination number in a given cell was determined as follows:

$$\langle CN\rangle = \frac{1}{N_p^c}\sum_{k=1}^{N_p^c} CN_k, \tag{53}$$

where N_p^c is the number of particles in the cell and CN_k is the coordination number of particle k. Similarly, the mean particle velocity in a particular cell was calculated as:

$$U_{p,i} = \frac{1}{N_p^c}\sum_{k=1}^{N_p^c} u_{k,i}, \tag{54}$$

where $u_{k,i}$ is the velocity of particle k. The solid volume fraction for a specific cell was obtained as follows:

$$\alpha_p = \frac{N_p^c v_p}{V_c}, \tag{55}$$

where V_c is the volume of the cell.

The time derivative in Eq. (52) was computed for a specific cell with a backward difference:

$$\left.\frac{\partial}{\partial t}\left(\alpha_p\langle CN\rangle\right)\right|_n = \frac{\left(\alpha_p\langle CN\rangle\right)|_n - \left(\alpha_p\langle CN\rangle\right)|_{n-1}}{\Delta t_g}, \tag{56}$$

where n and $n-1$ represent the current and previous states, respectively, and Δt_g stands for the gas time step.

The divergence in Eq. (52) was calculated by employing the Gauss–Ostrogradsky theorem. This theorem is given by:

$$\iint_S Q_i n_i\, dS = \iiint_V \frac{\partial Q_i}{\partial x_i}\, dV, \tag{57}$$

where V refers to the volume bounded by a surface S, Q_i represents a vector field, and n_i stands for the unit vector normal to S and oriented outward. Assuming that the spatial variation of $\partial Q_i/\partial x_i$ is negligible inside the volume V, the integral over V in Eq. (57) can be expressed as:

$$\iiint_V \frac{\partial Q_i}{\partial x_i}\, dV = \frac{\partial Q_i}{\partial x_i} V. \tag{58}$$

Assuming that the spatial variation of $Q_i n_i$ is negligible inside each face (part of the surface S), the integral over S in Eq. (57) can be formulated as:

$$\iint_S Q_i n_i\, dS = \sum_{j=1}^{N_f}\int_{S_j} Q_i n_i\, dS = \sum_{j=1}^{N_f} Q_{i,j} n_{i,j} S_j, \tag{59}$$

where N_f is the number of faces comprising the closed surface S, and S_j is the surface area of face j. Substituting Eqs. (58) and (59) into Eq. (57) gives:

$$\sum_{j=1}^{N_f} Q_{i,j} n_{i,j} S_j = \frac{\partial Q_i}{\partial x_i} V. \tag{60}$$

Then, the divergence of Q_i can be calculated in the following way:

$$\frac{\partial Q_i}{\partial x_i} = \frac{1}{V}\sum_{j=1}^{N_f} Q_{i,j} n_{i,j} S_j. \tag{61}$$

We used the face-to-element connectivity in YALES2, which enabled us to consider two adjacent cells and compute the flux between them (flux across a face). The value of $\alpha_p U_{p,i}\langle CN\rangle$ at a face j between two adjacent cells c_1 and c_2 was determined as follows:

$$\left(\alpha_p U_{p,i}\langle CN\rangle\right)_j = \frac{1}{2}\left[\left(\alpha_p U_{p,i}\langle CN\rangle\right)_{c_1} + \left(\alpha_p U_{p,i}\langle CN\rangle\right)_{c_2}\right]. \tag{62}$$

The divergence of $\alpha_p U_{p,i}\langle CN\rangle$ for a particular cell with volume V_c and N_f^c faces was computed as follows (see Eq. (61)):

$$\frac{\partial}{\partial x_i}\left(\alpha_p U_{p,i}\langle CN\rangle\right) = \frac{1}{V_c}\sum_{j=1}^{N_f^c}\left(\alpha_p U_{p,i}\langle CN\rangle\right)_j n_{i,j} S_j, \tag{63}$$

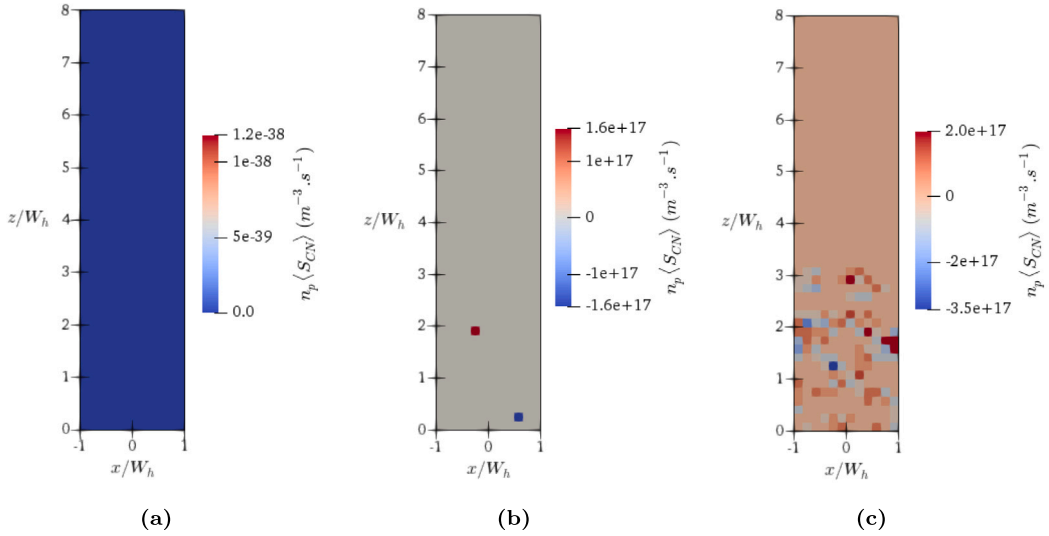

Fig. 16. Instantaneous distribution of the coordination number source term in the presence of adhesion at different superficial gas velocity values: (a) 0.97 mm/s (fixed bed), (b) 5.54 mm/s (expanded bed), and (c) 11.08 mm/s (bubbling bed).

where $\left(\alpha_p U_{p,i}\langle CN\rangle\right)_j$ was obtained from Eq. (62). With the mesoscopic Eulerian method, the source term is calculated using Eq. (52), where the time derivative and divergence terms are computed using Eqs. (56) and (63).

4.3. Results

Fig. 15 displays the distributions of the coordination number source term at a superficial gas velocity of 11.08 mm/s, obtained using the direct Lagrangian and mesoscopic Eulerian methods. The two distributions are identical, indicating consistency between the two methods. The positive source term values imply an increase in the coordination number, while the negative source term values imply a decrease in the coordination number.

Fig. 16 illustrates the distribution of the coordination number source term, computed using the direct Lagrangian method, for various inlet gas velocities during the fluidization cycle with adhesion. In the fixed bed regime, the coordination number source term is zero everywhere, indicating no change in the coordination number. In the expanded bed regime (homogeneous fluidization), the source term is non-zero in very few cells, and at certain times, it is zero in all cells. To demonstrate this regime adequately, we provide a representative source term distribution in Fig. 16(b). This distribution shows that there are slight variations in the coordination number in the homogeneous fluidization regime. In the bubbling bed regime, the local magnitudes of the source term are higher due to significant variations in the coordination number.

Fig. 17 shows the distributions of the coordination number source term at a superficial gas velocity of 5.54 mm/s for tests conducted with and without adhesion. Both Figs. 17(a) and 17(b) represent the same time instant. As observed, the local magnitudes of the coordination number source term in the absence of adhesion (no homogeneous fluidization regime) are significantly larger than those in the presence of adhesion (homogeneous fluidization). These distributions reveal that the coordination number varies considerably in the absence of adhesion compared to when adhesion is present.

The obtained measurements of the source term are essential for developing and validating a Eulerian model for it. The developed source term expression can then be used in two-fluid simulations to determine the evolution of the coordination number and predict the hysteresis in the bed pressure drop at the macroscale.

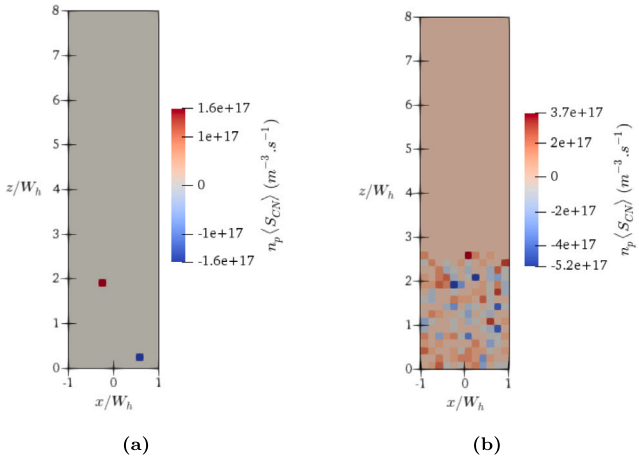

Fig. 17. Comparison of coordination number source term at a superficial gas velocity of 5.54 mm/s: (a) with vs. (b) without Van der Waals adhesion.

5. Conclusion

In this study, CFD-DEM simulations were conducted to predict the pressure-drop hysteresis phenomenon observed in fluidized beds of fine solids. In a fluidization test case without Van der Waals adhesion, an overshoot attributed to static wall friction was predicted. With adhesion, the intensity of the overshoot increased. A hysteresis in the pressure drop across the particle bed was observed. Furthermore, our results reveal that predicting the homogeneous bed expansion between the minimum fluidization and minimum bubbling velocities necessitates accounting for Van der Waals adhesion. The coordination number source term was shown to be affected by the superficial gas velocity and Van der Waals forces. In contrast to the case without Van der Waals adhesion, the presence of adhesion prevents significant variations in the coordination number when the superficial gas velocity is increased to a value between the minimum fluidization velocity and the bubbling threshold.

The new numerical data extracted from our CFD-DEM simulations may be utilized to guide the development and validation of an Eulerian model for adhesion and a continuum transport equation for the coordination number, enabling the prediction of pressure hysteresis using

two-fluid simulations.

Our fluidization and defluidization simulations did not use spring stiffness values obtained from real material properties, specifically Young's modulus and Poisson's ratio. Using these properties would result in a much higher spring stiffness value, leading to a considerably smaller contact duration and particle time step, which significantly increases the computational cost. A potential solution to reduce computational cost would be to implement the modified adhesion model suggested by Gu et al. [60], which allows the use of lower spring stiffness values than reality without affecting accuracy.

CRediT authorship contribution statement

Youssef Badran: Writing – original draft, Visualization, Validation, Software, Resources, Methodology, Investigation, Formal analysis, Data curation, Conceptualization. **Dorian Dupuy:** Writing – review & editing, Validation, Software, Resources, Methodology, Investigation. **Bruno Blais:** Writing – review & editing, Resources, Methodology, Investigation. **Vincent Moureau:** Writing – review & editing, Software, Resources, Methodology, Investigation. **Renaud Ansart:** Writing – review & editing, Supervision, Software, Resources, Project administration, Methodology, Investigation, Funding acquisition, Conceptualization. **Jamal Chaouki:** Writing – review & editing, Supervision, Resources, Methodology, Investigation, Funding acquisition, Formal analysis, Conceptualization. **Olivier Simonin:** Writing – review & editing, Validation, Supervision, Software, Resources, Methodology, Investigation, Conceptualization.

Declaration of competing interest

The authors declare that they have no known competing financial interests or personal relationships that could have appeared to influence the work reported in this paper.

Acknowledgments

The authors gratefully acknowledge the CORIA laboratory and the YALES2 community for providing the YALES2 code (CNRS deposit by Vincent Moureau, Ghislain Lartigue, and Pierre Benard). The authors would also like to acknowledge Dr. Yann Dufresne and Dr. Ainur Nigmetova for their valuable discussions on CFD-DEM modeling of fluid–particle flows. This project was provided with computing and storage resources by GENCI on the CSL/SKL partition of the Jean-Zay/Joliot-Curie supercomputer at IDRIS/TGCC thanks to grant A0142B06938, and by CALMIP through grant P1132.

Data availability

Data will be made available on request.

References

[1] J. Yates, J. Mullin, Fundamentals of fluidized-bed chemical processes: Butterworths monographs in chemical engineering, Butterworths monographs in chemical engineering, Elsevier Science, 2013, URL https://books.google.fr/books?id=NOQgBQAAQBAJ.

[2] D. Kunii, O. Levenspiel, Fluidization Engineering, Butterworth-Heinemann, 1991, URL https://books.google.ca/books?id=ZVnb17qRz8QC.

[3] A. Burggraeve, T. Monteyne, C. Vervaet, J.P. Remon, T. De Beer, Process analytical tools for monitoring, understanding, and control of pharmaceutical fluidized bed granulation: A review, Eur. J. Pharmaceut. Biopharmaceut. 83 (1) (2013) 2–15, URL https://doi.org/10.1016/j.ejpb.2012.09.008.

[4] S. Hovmand, Fluidized bed drying, in: Handbook of Industrial Drying, CRC Press, 2020, pp. 195–248, URL https://doi.org/10.1201/9780429289774.

[5] M.A. Acheampong, P.N. Lens, Treatment of gold mining effluent in pilot fixed bed sorption system, Hydrometall. 141 (2014) 1–7, URL https://doi.org/10.1016/j.hydromet.2013.10.013.

[6] W. Yang, Handbook of fluidization and fluid-particle systems, Chemical Industries, CRC Press, 2003, URL https://books.google.fr/books?id=lHTUphHZyogC.

[7] J.R. Grace, J. Chaouki, T. Pugsley, Fluidized bed reactor, Part. Technol. Appl. (2012) 199, URL https://books.google.fr/books?id=dznOBQAAQBAJ.

[8] D. Dupuy, Y. Badran, R. Ansart, O. Simonin, Calibrating the frictional-pressure model from two-fluid simulation of fluidised beds in the defluidisation regime, Powder Technol. 441 (2024) 119776, URL https://doi.org/10.1016/j.powtec.2024.119776.

[9] M. Zhang, K. Chu, F. Wei, A. Yu, A CFD–DEM study of the cluster behavior in riser and downer reactors, Powder Technol. 184 (2) (2008) 151–165, URL https://doi.org/10.1016/j.powtec.2007.11.036.

[10] S. Mutsers, K. Rietema, The effect of interparticle forces on the expansion of a homogeneous gas-fluidized bed, Powder Technol. 18 (2) (1977) 239–248, URL https://doi.org/10.1016/0032-5910(77)80014-4.

[11] S. Tsinontides, R. Jackson, The mechanics of gas fluidized beds with an interval of stable fluidization, J. Fluid Mech. 255 (1993) 237–274, URL https://doi.org/10.1017/S0022112093002472.

[12] K. Rietema, H. Piepers, The effect of interparticle forces on the stability of gas-fluidized beds—I. Experimental evidence, Chem. Eng. Sci. 45 (6) (1990) 1627–1639, URL https://doi.org/10.1016/0009-2509(90)80015-7.

[13] A. Srivastava, S. Sundaresan, Role of wall friction in fluidization and standpipe flow, Powder Technol. 124 (1–2) (2002) 45–54, URL https://doi.org/10.1016/S0032-5910(01)00471-5.

[14] B. Liu, X. Zhang, L. Wang, H. Hong, Fluidization of non-spherical particles: Sphericity, zingg factor and other fluidization parameters, Particuology 6 (2) (2008) 125–129, URL https://doi.org/10.1016/j.cpart.2007.07.005.

[15] F. Vanni, B. Caussat, C. Ablitzer, M. Brothier, Effects of reducing the reactor diameter on the fluidization of a very dense powder, Powder Technol. 277 (2015) 268–274, URL https://doi.org/10.1016/j.powtec.2015.03.010.

[16] S. Sánchez-Delgado, J.A. Almendros-Ibáñez, N. García-Hernando, D. Santana, On the minimum fluidization velocity in 2D fluidized beds, Powder Technol. 207 (1–3) (2011) 145–153, URL https://doi.org/10.1016/j.powtec.2010.10.020.

[17] H. Matuttis, S. Luding, H. Herrmann, Discrete element simulations of dense packings and heaps made of spherical and non-spherical particles, Powder Technol. 109 (1–3) (2000) 278–292, URL https://doi.org/10.1016/S0032-5910(99)00243-0.

[18] Y. Dufresne, V. Moureau, G. Lartigue, O. Simonin, A massively parallel CFD/DEM approach for reactive gas-solid flows in complex geometries using unstructured meshes, Comput. & Fluids 198 (2020) 104402, URL https://doi.org/10.1016/j.compfluid.2019.104402.

[19] J. Capecelatro, O. Desjardins, An Euler–Lagrange strategy for simulating particle-laden flows, J. Comput. Phys. 238 (2013) 1–31, URL https://doi.org/10.1016/j.jcp.2012.12.015.

[20] H. Neau, M. Pigou, P. Fede, R. Ansart, C. Baudry, N. Mérigoux, J. Laviéville, Y. Fournier, N. Renon, O. Simonin, Massively parallel numerical simulation using up to 36,000 CPU cores of an industrial-scale polydispersed reactive pressurized fluidized bed with a mesh of one billion cells, Powder Technol. 366 (2020) 906–924, URL https://doi.org/10.1016/j.powtec.2020.03.010.

[21] J.W. Landry, G.S. Grest, S.J. Plimpton, Discrete element simulations of stress distributions in silos: crossover from two to three dimensions, Powder Technol. 139 (3) (2004) 233–239, URL https://doi.org/10.1016/j.powtec.2003.10.016.

[22] S. Affleck, A. Thomas, A. Routh, N. Vriend, Novel protocol for quantifying powder cohesivity through fluidisation tests, Powder Technol. 415 (2023) 118147, URL https://doi.org/10.1016/j.powtec.2022.118147.

[23] I. Soleimani, N. Elahipanah, J. Shabanian, J. Chaouki, In-situ quantification of the magnitude of interparticle forces and its temperature variation in a gas-solid fluidized bed, Chem. Eng. Sci. 232 (2021) 116349, URL https://doi.org/10.1016/j.ces.2020.116349.

[24] M.W. Weber, C.M. Hrenya, Computational study of pressure-drop hysteresis in fluidized beds, Powder Technol. 177 (3) (2007) 170–184, URL https://doi.org/10.1016/j.powtec.2007.01.016.

[25] D. Dupuy, R. Ansart, O. Simonin, Investigation of near-wall particle statistics in CFD-DEM simulations of dense fluidised beds and derivation of an Eulerian particle dynamic wall boundary condition, J. Fluid Mech. 982 (2024) A2, URL https://doi.org/10.1017/jfm.2024.36.

[26] L. Rothenburg, N.P. Kruyt, Critical state and evolution of coordination number in simulated granular materials, Int. J. Solids Struct. 41 (21) (2004) 5763–5774, URL https://doi.org/10.1016/j.ijsolstr.2004.06.001.

[27] J. Sun, S. Sundaresan, A constitutive model with microstructure evolution for flow of rate-independent granular materials, J. Fluid Mech. 682 (2011) 590–616, URL https://doi.org/10.1017/jfm.2011.251.

[28] S. Chialvo, J. Sun, S. Sundaresan, Bridging the rheology of granular flows in three regimes, Phys. Rev. E 85 (2) (2012) 021305, URL https://doi.org/10.1103/PhysRevE.85.021305.

[29] S. Luding, Anisotropy in cohesive, frictional granular media, J. Phys.: Condens. Matter. 17 (24) (2005) S2623, URL https://doi.org/10.1088/0953-8984/17/24/017.

[30] Y. Gu, A. Ozel, J. Kolehmainen, S. Sundaresan, Computationally generated constitutive models for particle phase rheology in gas-fluidized suspensions, J. Fluid Mech. 860 (2019) 318–349, URL https://doi.org/10.1017/jfm.2018.856.

[31] Q. Hou, Z. Zhou, A. Yu, Micromechanical modeling and analysis of different flow regimes in gas fluidization, Chem. Eng. Sci. 84 (2012) 449–468, URL https://doi.org/10.1016/j.ces.2012.08.051.
[32] A. Vijayan, Y. Gan, R.K. Annabattula, Evolution of fabric in spherical granular assemblies under the influence of various loading conditions through DEM, Granul. Matter 22 (2020) 1–15, URL https://doi.org/10.1007/s10035-020-1000-9.
[33] R. Sun, H. Xiao, Diffusion-based coarse graining in hybrid continuum–discrete solvers: Theoretical formulation and a priori tests, Int. J. Multiph. Flow 77 (2015) 142–157, URL https://doi.org/10.1016/j.ijmultiphaseflow.2015.08.014.
[34] A. Nigmetova, E. Masi, O. Simonin, Y. Dufresne, V. Moureau, Three-dimensional DEM-CFD simulation of a lab-scale fluidized bed to support the development of two-fluid model approach, Int. J. Multiph. Flow 156 (2022) 104189, URL https://doi.org/10.1016/j.ijmultiphaseflow.2022.104189.
[35] Y. Dufresne, Développement D'un Solveur 3D Massivement Parallèle Pour La Prédiction D'écoulements Granulaires Réactifs En Géométrie Complexe (Ph.D. thesis), Normandie, 2019, URL https://theses.hal.science/tel-02924453.
[36] P. Costa, B.J. Boersma, J. Westerweel, W.-P. Breugem, Collision model for fully resolved simulations of flows laden with finite-size particles, Phys. Rev. E 92 (5) (2015) 053012, URL https://doi.org/10.1103/PhysRevE.92.053012.
[37] M.A. van der Hoef, M. Ye, M. van Sint Annaland, A. Andrews, S. Sundaresan, J. Kuipers, Multiscale modeling of gas-fluidized beds, Adv. Chem. Eng. 31 (2006) 65–149, URL https://doi.org/10.1016/S0065-2377(06)31002-2.
[38] V. Moureau, P. Domingo, L. Vervisch, Design of a massively parallel CFD code for complex geometries, C. R. Mec. 339 (2–3) (2011) 141–148, URL https://doi.org/10.1016/j.crme.2010.12.001.
[39] Z. Hamidouche, Y. Dufresne, J.-L. Pierson, R. Brahem, G. Lartigue, V. Moureau, DEM/CFD simulations of a pseudo-2D fluidized bed: Comparison with experiments, Fluids 4 (1) (2019) 51, URL https://doi.org/10.3390/fluids4010051.
[40] V. Komiwes, P. Mege, Y. Meimon, H. Herrmann, Simulation of granular flow in a fluid applied to sedimentation, Granul. Matter 8 (2006) 41–54, URL https://doi.org/10.1007/s10035-005-0220-3.
[41] S. Golshan, P. Munch, R. Gassmöller, M. Kronbichler, B. Blais, Lethe-DEM: An open-source parallel discrete element solver with load balancing, Comput. Part. Mech. 10 (1) (2023) 77–96, URL https://doi.org/10.1007/s40571-022-00478-6.
[42] M. Elimelech, J. Gregory, X. Jia, Particle Deposition and Aggregation: Measurement, Modelling and Simulation, Butterworth-Heinemann, 2013, URL https://books.google.ca/books?id=R6g3BQAAQBAJ.
[43] O.R. Walton, Numerical simulation of inelastic, frictional particle-particle interactions, Part. Two- Phase Flow 25 (1993) 884–911.
[44] M. Sperl, Experiments on corn pressure in silo cells–translation and comment of janssen's paper from 1895, Granul. Matter 8 (2) (2006) 59–65, URL https://doi.org/10.1007/s10035-005-0224-z.
[45] A. Anand, J.S. Curtis, C.R. Wassgren, B.C. Hancock, W.R. Ketterhagen, Predicting discharge dynamics from a rectangular hopper using the discrete element method (DEM), Chem. Eng. Sci. 63 (24) (2008) 5821–5830, URL https://doi.org/10.1016/j.ces.2008.08.015.
[46] P. Kosinski, A.C. Hoffmann, Extended hard-sphere model and collisions of cohesive particles, Phys. Rev. E— Stat. Nonlinear Soft Matter Phys. 84 (3) (2011) 031303, URL https://doi.org/10.1103/PhysRevE.84.031303.
[47] M. Mihajlovic, I. Roghair, M.V.S. Annaland, On the numerical implementation of the Van der Waals force in soft-sphere discrete element models for gas-solid fluidization, Chem. Eng. Sci. 226 (2020) 115794, URL https://doi.org/10.1016/j.ces.2020.115794.
[48] M. Ye, M.A. van der Hoef, J. Kuipers, The effects of particle and gas properties on the fluidization of geldart a particles, Chem. Eng. Sci. 60 (16) (2005) 4567–4580, URL https://doi.org/10.1016/j.ces.2005.03.017.
[49] M. Kraushaar, Application of the Compressible and Low-Mach Number Approaches to Large-Eddy Simulation of Turbulent Flows in Aero-Engines (Ph.D. thesis), 2011, URL https://oatao.univ-toulouse.fr/6921/.
[50] R.D. Groot, P.B. Warren, Dissipative particle dynamics: Bridging the gap between atomistic and mesoscopic simulation, J. Chem. Phys. 107 (11) (1997) 4423–4435, URL https://doi.org/10.1063/1.474784.
[51] A. Gobin, H. Neau, O. Simonin, J.-R. Llinas, V. Reiling, J.-L. Sélo, Fluid dynamic numerical simulation of a gas phase polymerization reactor, Internat. J. Numer. Methods Fluids 43 (10–11) (2003) 1199–1220, URL https://doi.org/10.1002/fld.542.
[52] S. Ergun, Fluid flow through packed columns, Chem. Eng. Prog. 48 (2) (1952) 89, URL https://cir.nii.ac.jp/crid/1572261550410403712.
[53] C. Wen, Y. Yu, A generalized method for predicting the minimum fluidization velocity, AIChE J. 12 (3) (1966) 610–612, URL https://doi.org/10.1002/aic.690120343.
[54] O. Simonin, S. Chevrier, F. Audard, P. Fede, Drag force modelling in dilute to dense particle-laden flows with mono-disperse or binary mixture of solid particles, in: 9th International Conference on Multiphase Flow (ICMF 2016), 2016, pp. pp–1, URL https://hal.science/hal-01706862v1/file/Simonin_19509.pdf.
[55] A.R. Abrahamsen, D. Geldart, Behaviour of gas-fluidized beds of fine powders part I. Homogeneous expansion, Powder Technol. 26 (1) (1980) 35–46, URL https://doi.org/10.1016/0032-5910(80)85005-4.
[56] J. Zhang, T. Majmudar, A. Tordesillas, R. Behringer, Statistical properties of a 2D granular material subjected to cyclic shear, Granul. Matter 12 (2010) 159–172, URL https://doi.org/10.1007/s10035-010-0170-2.
[57] M. Lätzel, S. Luding, H.J. Herrmann, Macroscopic material properties from quasi-static, microscopic simulations of a two-dimensional shear-cell, Granul. Matter 2 (2000) 123–135, URL https://doi.org/10.1007/s100350000048.
[58] P.N. Loezos, P. Costamagna, S. Sundaresan, The role of contact stresses and wall friction on fluidization, Chem. Eng. Sci. 57 (24) (2002) 5123–5141, URL https://doi.org/10.1016/S0009-2509(02)00421-9.
[59] Y. Badran, R. Ansart, J. Chaouki, O. Simonin, Macro-scale numerical investigation of the contribution of Van der Waals force to the pressure-drop overshoot in fine-particle fluidized beds, Powder Technol. 436 (2024) 119505, URL https://doi.org/10.1016/j.powtec.2024.119505.
[60] Y. Gu, A. Ozel, S. Sundaresan, A modified cohesion model for CFD–DEM simulations of fluidization, Powder Technol. 296 (2016) 17–28, URL https://doi.org/10.1016/j.powtec.2015.09.037.